



AFRL-AFOSR-JP-TR-2019-0030

Integration of Experiment and Modelling to Advance Biosensor
Design based on Conformational Switching of Surface-Adsorbed
Nucleic Acids.

Tiffany Walsh
DEAKIN UNIVERSITY
221 BURWOOD HWY
BURWOOD, 3125
AU

04/29/2019
Final Report

DISTRIBUTION A: Distribution approved for public release.

Air Force Research Laboratory
Air Force Office of Scientific Research
Asian Office of Aerospace Research and Development
Unit 45002, APO AP 96338-5002

REPORT DOCUMENTATION PAGE					Form Approved OMB No. 0704-0188	
<p>The public reporting burden for this collection of information is estimated to average 1 hour per response, including the time for reviewing instructions, searching existing data sources, gathering and maintaining the data needed, and completing and reviewing the collection of information. Send comments regarding this burden estimate or any other aspect of this collection of information, including suggestions for reducing the burden, to Department of Defense, Executive Services, Directorate (0704-0188). Respondents should be aware that notwithstanding any other provision of law, no person shall be subject to any penalty for failing to comply with a collection of information if it does not display a currently valid OMB control number.</p> <p>PLEASE DO NOT RETURN YOUR FORM TO THE ABOVE ORGANIZATION.</p>						
1. REPORT DATE (DD-MM-YYYY) 29-04-2019		2. REPORT TYPE Final		3. DATES COVERED (From - To) 08 Jul 2016 to 07 Jan 2019		
4. TITLE AND SUBTITLE Integration of Experiment and Modelling to Advance Biosensor Design based on Conformational Switching of Surface-Adsorbed Nucleic Acids.				5a. CONTRACT NUMBER		
				5b. GRANT NUMBER FA2386-16-1-4053		
				5c. PROGRAM ELEMENT NUMBER 61102F		
6. AUTHOR(S) Tiffany Walsh				5d. PROJECT NUMBER		
				5e. TASK NUMBER		
				5f. WORK UNIT NUMBER		
7. PERFORMING ORGANIZATION NAME(S) AND ADDRESS(ES) DEAKIN UNIVERSITY 221 BURWOOD HWY BURWOOD, 3125 AU				8. PERFORMING ORGANIZATION REPORT NUMBER		
9. SPONSORING/MONITORING AGENCY NAME(S) AND ADDRESS(ES) AOARD UNIT 45002 APO AP 96338-5002				10. SPONSOR/MONITOR'S ACRONYM(S) AFRL/AFOSR IOA		
				11. SPONSOR/MONITOR'S REPORT NUMBER(S) AFRL-AFOSR-JP-TR-2019-0030		
12. DISTRIBUTION/AVAILABILITY STATEMENT A DISTRIBUTION UNLIMITED: PB Public Release						
13. SUPPLEMENTARY NOTES						
14. ABSTRACT <p>The PI has had very good success with this grant. The ability to reliably detect stress indicators at the molecular level in the body is a key strategy in managing warfighter performance. There is a huge need in the Air Force to monitor levels of warfighter stress, vigilance and fatigue in warfighters, in-situ. By accomplishing this goal, degradation in operator performance can then be addressed and consequently managed. The detection of molecules that are produced in the body in response to stress, known as molecular stress biomarkers, is a viable strategy for achieving this. One approach for detecting these biomarkers is to exploit the recognition capabilities of nucleic acid aptamers, to construct bio-sensors based on these aptamers denoted herein as aptasensors. One of the key challenges inherent to the design and implementation of these aptasensors is the lack of direct structural evidence at the molecular-level regarding the conformations of the aptamer when adsorbed at the aqueous substrate, in both the presence and the absence of the target analyte. Our overall aim in this project is to establish this fundamental understanding via use of molecular dynamics (MD) simulations, in partnership with complementary experimental data, and to thereby enable the realization of reliable aptasensors based on graphene and Au nanoparticle substrates. There were 4 peer reviewed publications as a direct result of this grant funding.</p>						
15. SUBJECT TERMS Adsorption, Aptamers, Assay, Biomarkers, Binding, Simulation, Human Performance, Sensing, Molecular Dynamics						
16. SECURITY CLASSIFICATION OF:			17. LIMITATION OF ABSTRACT SAR	18. NUMBER OF PAGES	19a. NAME OF RESPONSIBLE PERSON CHEN, JERMONT	
a. REPORT Unclassified	b. ABSTRACT Unclassified	c. THIS PAGE Unclassified			19b. TELEPHONE NUMBER (Include area code) 315-227-7007	

AOARD Final Report

Contract/Grant Title: Integration of Experiment and Modelling to Advance Biosensor Design based on Conformational Switching of Surface-Adsorbed Nucleic Acids

Contract/Grant#: FA2386-16-1-4053

Period of Performance: 01 July 2016 – 30 Nov 2018

Budget for period of performance: \$100 K

Program Officer: Dr. Jermont Chen

Principal Investigator: Prof. Tiffany R. Walsh,
Institute for Frontier Materials,
Deakin University, Geelong VIC 3216, Australia
Phone: +61 (352) 273 116
Email: tiffany.walsh@deakin.edu.au

A. Executive Summary:

Overview of Key Concepts

Project Summary

External Collaborations

New Publications

B.1. Calibration and validation of interatomic potentials for DNA/substrate interactions

B.2. Structural disruption of an adenosine-binding DNA aptamer adsorbed on graphene

B.3. Structural predictions of the MN4 aptamer in the presence and absence of cocaine.

B.4. Conformational disruption of the MN4 aptamer adsorbed on Au nanoparticle in the presence and absence of cocaine.

C. Summary and Outlook

A. Executive Summary:

Overview of Key Concepts: An aptamer is a nucleic acid (NA) sequence (typically DNA or RNA) that can bind a target molecular analyte with very high specificity and sensitivity, which takes place via the

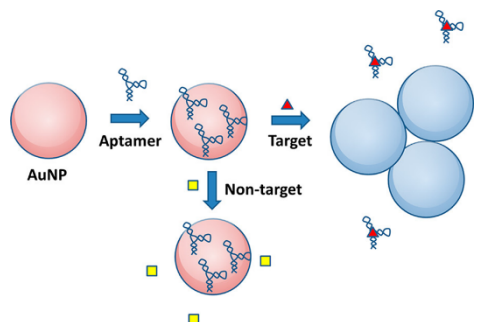


Figure A.1.1. Schematic of the AuNP/apptamer/target system. The aptamer-target binding event leads to a **proposed** conformational change that results in desorption of the aptamer from the Au NP surface, and subsequent aggregation of the Au NPs. Reproduced from Mirau et al., Ref 3.

structural rearrangement of the NA into a binding conformation that matches the electronic and structural features of the analyte. The use of aptamers, as opposed to other types of recognition elements, such as antibodies, confers distinct advantages, including facile synthesis and durability. Aptamers can be combined with a reporting element, in this case, Au nanoparticles (Au NPs)¹ or graphene substrates. For example, as illustrated in **Figure A.1.1**, in general, colorimetric sensors based on Au NPs operate by modulating the propensity for the Au NPs to aggregate in solution when subjected to salt challenge (an increase in the concentration of salt in solution required to trigger the onset of aggregation). Dispersed (un-aggregated) Au NP solutions display a red-pink color, while aggregation induces a purple-blue color. These color changes are visible to the naked eye.

Project Summary: The ability to reliably detect stress indicators at the molecular level in the body is a key strategy in managing warfighter performance. There is a huge need in the Air Force to monitor levels of warfighter stress, vigilance and fatigue in warfighters, *in-situ*. By accomplishing this goal, degradation in operator performance can then be addressed and consequently managed. The detection of molecules that are produced in the body in response to stress, known as molecular stress biomarkers, is a viable strategy for achieving this. One approach for detecting these biomarkers is to exploit the recognition capabilities of nucleic acid aptamers, to construct bio-sensors based on these aptamers denoted herein as aptasensors. ***One of the key challenges inherent to the design and implementation of these aptasensors is the lack of direct structural evidence at the molecular-level regarding the conformations of the aptamer when adsorbed at the aqueous substrate, in both the presence and the absence of the target analyte.*** Our overall aim in this project is to establish this fundamental understanding *via* use of molecular dynamics (MD) simulations, in partnership with complementary experimental data, and to thereby enable the realization of reliable aptasensors based on graphene and Au nanoparticle substrates.

In this two-year project, we have pursued four systematic steps towards realizing this goal. In Phase 1 (**Section B1**) we investigated and verified the use of our inter-atomic potentials to describe the aptamer/substrate interface under aqueous conditions. In Phase 2 (**Section B2**) we leveraged existing the wealth of experimental structural data to investigate if our MD simulations could recover experimentally observed behaviors of the adenosine-binding aptamer when interfaced with the aqueous graphene interface. Phase 3 (**Sections B3 and B4**), enabled us, in collaboration with AFRL researchers, to explore the exemplar system for Au nanoparticle based colorimetric sensors, based on the cocaine-binding MN4 aptamer.

New Publications:

1. Z. E. Hughes, G. Wei, K. L. M. Drew, L. Colombi Ciacchi, and T. R. Walsh* “Adsorption of DNA Fragments at Aqueous Graphene and Au(111) *via* Integration of Experiment and Simulation”, *Langmuir*, **2017**, 33, 10193-10204.
2. Z. E. Hughes and T. R. Walsh*, “Structural Disruption of an Adenosine-Binding DNA Aptamer Adsorbed on Graphene”, *ACS Sensors*, **2017**, 2, 1602-1611.
3. A. Budi, B. Demir, N. M. Bedford, J. L. Chavez, P. A. Mirau and T. R. Walsh*, “Revealing the recognition mechanism for the cocaine-binding aptamer MN4”, in preparation for submission to *Nucleic Acids Research*.
4. A. Budi, B. Demir and T. R. Walsh*, “Conformational disruption of the MN4 aptamer adsorbed on Au nanoparticle in the presence and absence of cocaine”, in preparation for submission to *Langmuir*.

Collaborations:

Dr. Jorge Chavez (711 HPW/RHXBC, AFRL WPAFB) – Experimental investigation of aptamer performance for aptamer/Au nanoparticle systems in aqueous media.

Dr. Peter Mirau (RXAS, AFRL WPAFB) – Experimental nuclear magnetic resonance studies of aptamer structure at the molecular level.

Prof. Lucio Colombi Ciacchi (Dept. of Production Engineering, University of Bremen, Germany) – Experimental single molecule force spectroscopy studies to quantify interaction strengths of nucleic acid fragments on Au and graphene substrates.

Prof. Chang-Guo Zhan (College of Pharmacy, University of Kentucky, USA) – Prof. Zhan has kindly shared his AMBER parametrization of the cocaine molecule with me, to enable simulations of the MN4 (cocaine-binding) aptamer.

Dr. Nick Bedford (formerly RXAS, AFRL WPAFB; currently at University of New South Wales, Sydney, Australia) – experimental SAXS characterization of the structure of the MN4 aptamer.

Prof. Ewa Goldys and Dr. Guozhen Liu (Graduate School of Biomedical Engineering, University of New South Wales, Sydney, Australia) – Experimental characterization of performance of IgE-binding aptamers grafted on Au nanoparticles.

B.1. Calibration and validation of interatomic potentials for DNA/substrate interactions

To drive aptasensor technologies further, a deeper comprehension of the relationship between the properties of these interfacial systems and the structural traits of the adsorbed aptamers is required. Atomic force microscopy (AFM) based single molecule force spectroscopy (SMFS) provide a means by which the adsorption force of a molecule to a solid surface (substrate) may be measured under aqueous conditions, providing information about these interfacial interactions. By performing SMFS experiments under different conditions, valuable insights into the interactions of the aptamer with the substrate can be obtained.² However, while changes in the measured forces can be observed *via* SMFS, it is challenging to relate such differences to specific changes in the structure of the adsorbed aptamers using experimental techniques alone. Molecular dynamics (MD) simulations provide an approach by which the structure of aptamers adsorbed at aqueous interfaces can be investigated, allowing links to be made between the structure of an adsorbed aptamer and the properties of the system.

However, one of the challenges that has traditionally limited the ability of MD simulations to elucidate significant insights into biotic/abiotic interfaces has been the ensuring that the interatomic potential (herein referred to as a force-field, FF) used in these simulations can describe the interaction of the biomolecule with the aqueous substrate appropriately. To overcome this limitation, several recently-developed FFs have been specifically parametrized to capture the interactions of peptides with metallic and graphitic surfaces. However, a similar effort for nucleic acid/solid surface interactions has not yet been a focus. Moreover, a general lack of comprehensive experimental data available for comparison with molecular simulation, such as the free energy of adsorption of nucleic acid fragments, means that the validation, and systematic improvement, of these FFs remains a major challenge.

In this phase of the project, by combining molecular simulation with experimental SMFS measurements we seek to make connections between experiment, theory and simulation, providing mutual support for each. In the present work, our experimental collaborators (Colombi Ciacchi and co-workers) provided estimates of the free energy of adsorption per nucleotide at two substrates, Au(111) (we emphasize here that the SMFS experiments were conducted for the Au(111) surface and not the poly-crystalline Au surface) and graphite/graphene (herein referred to as C(0001), using SMFS measurements. These experimentally-derived free energy values were compared against those obtained from our metadynamics simulations of the nucleobases, nucleosides and nucleotides to the aqueous Au(111) and C(0001) interfaces. Overall, we found reasonable agreement in the trends between the experimental and computational results, providing validation for both.

Methods. The free energy of adsorption of the relevant nucleic acids to C(0001) and the Au(111) surface under aqueous conditions were predicted using well-tempered metadynamics³ simulations. The free energies were calculated for the four naturally-occurring DNA bases; adenine, cytosine, guanine and thymine, at the nucleobase, nucleoside and nucleotide level. The CHARMM29 FF parameters were used to model these molecules, and the modified version of TIP3P, compatible with the CHARMM FF, used to model liquid water. The interactions between the nucleic acids and the solvent with the substrates were described using the GoIP-CHARMM⁴ and GRAPPA⁵ FFs for Au(111) and C(0001), respectively. For the Au(111) substrate, a gold slab measuring $58.6 \times 60.9 \text{ \AA}$ and five atoms thick was used. These systems were modeled in liquid water, each system containing ~ 4900 water molecules and with the periodic distance between Au surfaces of $\approx 44 \text{ \AA}$. For C(0001), each system consisted of two graphene sheets $44.27 \times 38.34 \text{ \AA}$, separated by 48 \AA of liquid water and 36 \AA of vacuum. Each system contained 2546

water molecules. For the C(0001) interface, we considered two different solvent environments; liquid water (with a single Na^+ as a counter-ion for the nucleotides), and 0.16 mol kg^{-1} NaCl solution. For both the graphene and Au interfaces, the number of water molecules in the system was such to yield a bulk density of water in the center of the inter-slab space equivalent to that of a simulation cell of bulk water at the same ambient temperature and pressure.

Our simulations were performed using GROMACS version 4.5.5 with version 1.3 of the PLUMED plugin. The Lennard-Jones (LJ) non-bonded interactions were smoothly tapered to zero between 1.0 and 1.1 Å, and the electrostatic interactions were evaluated using a particle-mesh Ewald summation, with a real space cutoff of 1.3 Å. The simulations were performed in the canonical (NVT) ensemble, with the temperature maintained at 300 K through the use of the Nose-Hoover thermostat, with a coupling constant of 0.2 ps. In all simulations the collective variable upon which the bias was applied was the position of the center of mass of the adsorbate along the z-axis (*i.e.* the direction perpendicular to the substrate surface). Gaussians of 0.5 Å width were deposited every 1 ps, for a total simulation time of 150 ns for the nucleobases, and 350 ns for the nucleosides and nucleotides. The initial Gaussian height was set to 0.2 kJ mol^{-1} and a well-tempered metadynamics bias factor of 10 was used. The resulting free energy profiles were integrated to yield the free energy of adsorption.

Results and Discussion. Table B.1.1 summarizes the free energies of adsorption for all the DNA fragments to the aqueous C(0001) and Au(111) interfaces. **Figure B.1.1** shows the free energy profiles

Table B.1.1 Free energies of adsorption of the DNA fragments to the substrates in aqueous solution determined from metadynamics simulations. Comparison with nucleotide-level data from SMFS experiments provided for convenience.

Surface	Species	$\Delta \text{FE} / \text{kJ mol}^{-1}$			
		Nucleobase	Nucleoside	Nucleotide	Experiment
C(0001)	A	-22.5 ± 1.0	-25.2 ± 2.1	-27.1 ± 2.5	38 ± 5
	C	-12.9 ± 0.9	-18.0 ± 2.5	-21.4 ± 1.0	33 ± 8
	G	-27.7 ± 1.6	-31.5 ± 1.7	-38.3 ± 2.0	53 ± 11
	T	-16.5 ± 1.0	-23.1 ± 1.6	-27.9 ± 1.7	32 ± 3
Au(111)	A	-35.4 ± 1.8	-39.4 ± 1.8	-45.7 ± 3.1	36 ± 11
	C	-18.5 ± 1.0	-26.8 ± 1.7	-34.9 ± 1.3	28 ± 2
	G	-34.6 ± 1.1	-38.1 ± 0.9	-44.4 ± 1.3	29 ± 3
	T	-18.3 ± 0.5	-21.8 ± 0.9	-28.6 ± 1.5	21 ± 7

and convergence of the free energy as a function of simulation time for guanine, as an exemplar case, at the Au(111) and C(0001) interfaces.

At the aqueous C(0001) interface, by 150 ns of metadynamics simulations the free energy of the nucleobases had converged, as indicated in **Figure B.1.1(a)**. The free energy profile, **Figure B.1.1(b)**, exhibited a sharp minimum ~ 3.8 Å from the surface, and a local minimum located approximately 7 Å from the surface. There is a small barrier between the two minima, which we ascribe to the displacement of the first layer of interfacial water adsorbed at the aqueous interface (similar structuring was observed for the adsorption of amino acids at the aqueous C(0001) interface in earlier work). All of the nucleobases showed a strong binding affinity to the C(0001) interface, with the free energies of adsorption ranging from -13 to -30 kJ mol^{-1} . The rank ordering of the binding affinities for the

nucleobases to C(0001) under aqueous conditions was predicted to be $G > A > T > C$. This is the same rank ordering predicted by first principles and FF calculations for the adsorption of the nucleobases to C(0001) in *in vacuo*.

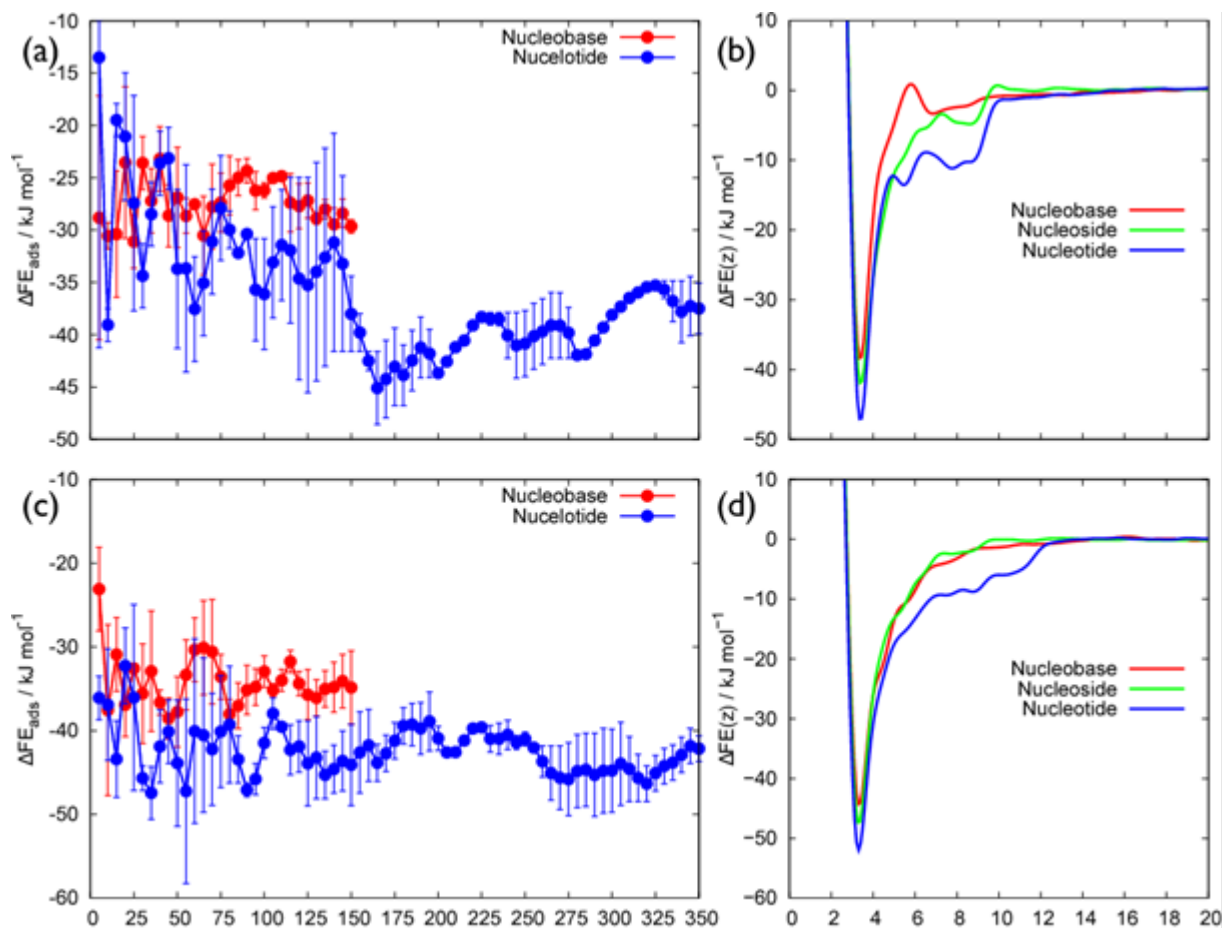


Figure B.1.1. Free energy of adsorption as a function of simulation time for the guanine nucleobase and nucleotide at (a) the aqueous C(0001) and (c) the aqueous Au(111) interfaces. Free energy profiles of the adsorption of the guanine nucleobase, nucleoside and nucleotide to (b) the aqueous C(0001) and (d) the aqueous Au(111) interfaces calculated from metadynamics simulations.

The addition of the deoxyribose sugar ring had a non-negligible effect on the free energy profiles (**Figure B.1.1b**). While the position of the global minimum was unchanged, the profile was much deeper ($\sim -5 \text{ kJ mol}^{-1}$) at a distance 5-10 Å from the C(0001) surface. These changes in the free energy profiles produced an increase in the absolute values of the free energy of adsorption of the nucleosides compared to the nucleobases. Compared against the nucleobases, the rank ordering in the binding affinities of the nucleosides was altered. While G and C were still the strongest and weakest adsorbing species, respectively, the differences between A and T was diminished, such that their binding free energies no longer differed significantly.

The more complex potential energy landscape of the adsorbed nucleotides made it more challenging to converge the adsorption free energies; however, by 350 ns of metadynamics simulations the free energies were reasonably equilibrated, as indicated in **Figure B.1.1a**). While the free energy profiles of the nucleotides differed from those of the nucleosides, the difference was not as pronounced

as between the nucleosides and the nucleobases (**Figure B.1.1b**). The predicted binding affinities of the nucleotides were stronger than those of the nucleosides. However, the relative ordering the nucleotides of $G > A \approx T > C$ remained the same, compared with the nucleosides. The presence of NaCl in the solvent did not appear to produce any meaningful differences in either the absolute adsorption free or the corresponding free energy profiles. This finding is despite the fact that the density of salt ions within 15Å of the substrate surface was greater than that in the bulk.

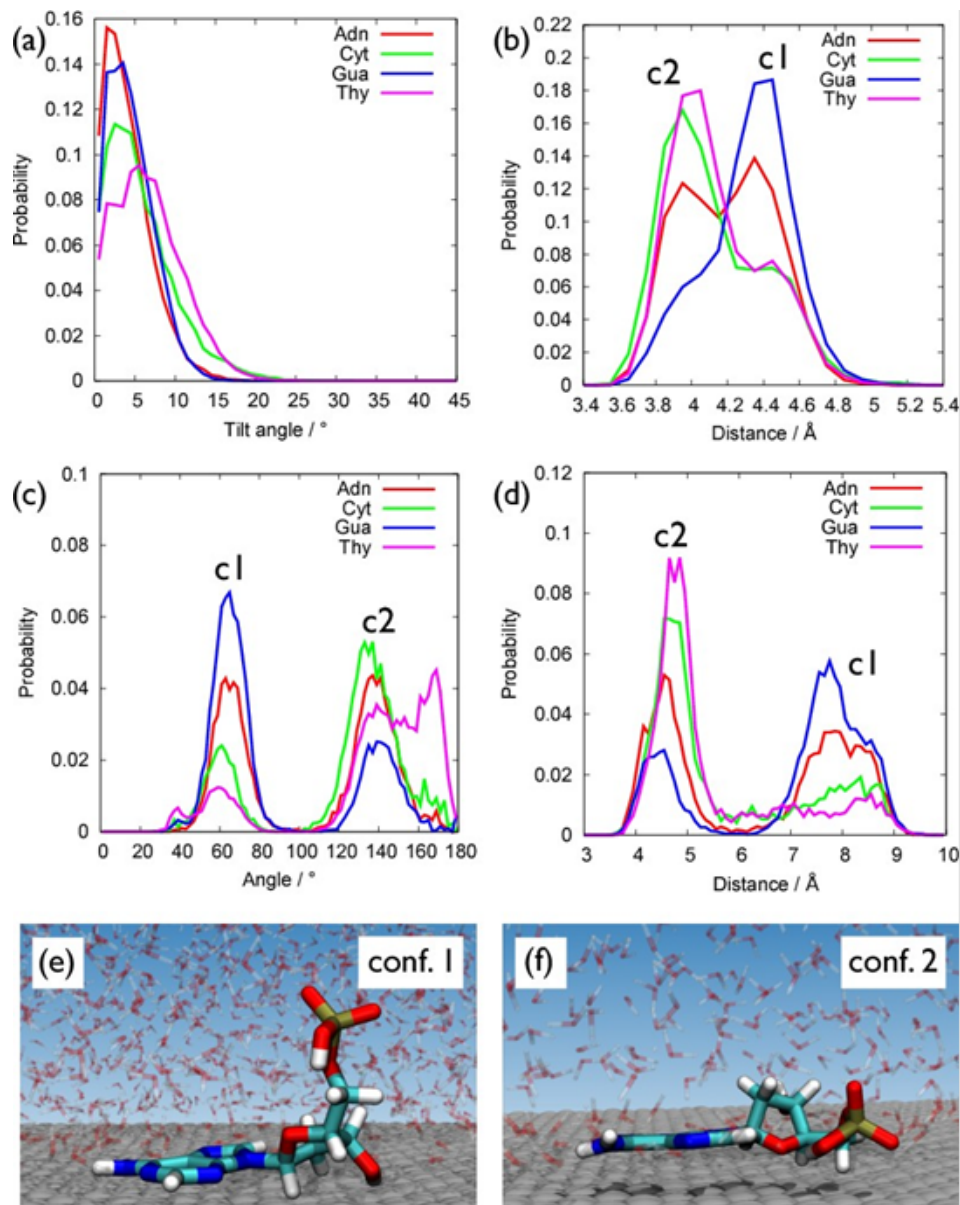


Figure B.1.2. Structural data of nucleotides adsorbed at the aqueous C(0001) interface: (a)-(d) Probability distributions of (a) the tilt angle of nucleobase ring with the C(0001) plane, (b) the of distance between the center of mass of deoxyribose ring and the C(0001) interface, (c) the orientation of the deoxyribose ring with the interface normal and (d) the distance between the phosphorous atom and the C(0001) interface. (e) and (f) Representative snapshots of deoxyadenosine monophosphate adsorbed at the aqueous C(0001) interface. The c1 and c2 notation on (b), (c), and (d) refers to conformations 1 and 2 shown in (e) and (f).

As at the C(0001) interface, the adsorption free energies of the nucleobases at Au(111) reached a converged value relatively quickly, but the nucleosides and nucleotides required much longer metadynamics simulation times, shown in **Figure B.1.1c**. In contrast to C(0001), the adsorption free energy profiles of the nucleobases at the aqueous Au(111) interface (**Figure B.1.1d**) showed only very minor barriers at the position corresponding with the first solvation layer. The adsorption free energies of the different nucleobases at the Au surface was less distinct than in the case of C(0001). While the purines ($\Delta FE_{\text{ads}} \approx -35 \text{ kJ mol}^{-1}$) adsorbed significantly more strongly than the pyrimidines ($\Delta FE_{\text{ads}} \approx -18 \text{ kJ mol}^{-1}$), there was no significant differences in binding strength between A and T, or G and C.

The significantly stronger adsorption of the purines remained in the case of the nucleosides and nucleotides (**Table B.1.1**), with A and G adsorbing approximately equally as strongly. In the case of the pyrimidines, the adsorption of T was slightly weaker than that of C at the nucleoside/tide level, giving a relative ordering of $G \approx A > C > T$. Unlike for the C(0001) interface, the adsorption free energy profiles of the nucleosides were not markedly broader than that of the nucleobases, although the addition of the phosphate group did induce some broadening. The depth of the free energy minimum increased with the size of the nucleic acid fragment.

There were two adsorbed conformations of the nucleotides at the C(0001) interface, as shown in **Figure B.1.2**. Both conformations featured the aromatic ring adsorbed flat the surface, but with different arrangements of the sugar ring and phosphate group. In conformation 1, the position/orientation of the deoxyribose ring was analogous to that of the nucleosides, while the phosphate group was located 8 Å from the surface, presented to the solution. In the case of conformation 2, the phosphate group was in direct contact with the C(0001) interface and the orientation vector of the deoxyribose ring was at an angle of $\sim 140^\circ$ to the surface normal. The relative populations of the two conformations depended on the base. For G, conformation 1 was favored, for C and T conformation 2 was more likely, and for A the two conformations were approximately equally probable. At the Au(111) interface, the two adsorbed conformations of the nucleotides were analogous to those found at the C(0001) interface. Again G showed a preference for a conformation with the phosphate group projected away from the surface, while T showed a preference for a conformation with the phosphate group close to the surface, and A and C did not show a preference for one conformation over the other.

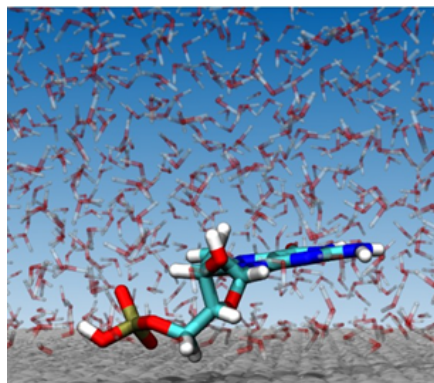


Figure B.1.3. Snapshot of a representative conformation of the guanine nucleotide at the aqueous C(0001) interface, corresponding with the local minimum at $\sim 8 \text{ Å}$ from the surface.

One of the challenges in drawing meaningful connections between the simulation and experimental data is that the experiments made use of 30 base ssDNA adsorbates, while the simulations were performed on individual nucleobases, nucleosides and nucleotides. Given that our simulation results suggested that different nucleotides yielded different proportions of the types of adsorbed conformation, the effect of neighboring nucleotides on the adhesion force of the ssDNA (and therefore their adsorption free energies) could vary with homo-oligomer. Thus, individual (free) nucleotides might assume adsorbed conformations that may not be relevant when part of an ssDNA oligomer. For example, the adsorption free energy profiles of the nucleotides (and the nucleosides in the case of C(0001)) obtained from our metadynamics simulations exhibit a minimum of ~ -10

kJ mol^{-1} at a distance $\sim 8 \text{ \AA}$ from the surface. A representative snapshot of the adsorbed nucleotides corresponding with this minimum is provided in **Figure B.1.3**, showing the deoxyribose and phosphate groups directly adsorbed at the substrate surface, with the nucleobase positioned above the first layer of bound water molecules. The SMFS measurements may not capture this local minimum (due to the aforementioned differences in the adsorption of a homo-oligomeric chain and the adsorption of a nucleotide) which could lead to discrepancies between the free energies estimated both by experiment and simulation. Moreover, the use of isolated nucleobases/tides/sides in our simulations will not capture effects arising from the formation of secondary structure in the ssDNA oligomers. Such secondary structure may influence the peeling force measured for the desorption of the ssDNA from the substrate. For dA_{30} , dC_{30} and dT_{30} this is less likely to be a serious consideration, but may be relevant for dG_{30} . Guanine-rich DNA sequences are known to support the formation of G-quartets, and, in some cases, may form quadruplex structures.

An evident and interesting difference between C(0001) and Au(111) emerged from both experiments and simulations, namely the stronger relative adsorption of A on Au(111) than on C(0001) with respect to the other bases. Our conformational analysis of the structures corresponding with the global minimum on the free energy (FE) surface suggested that both G and A assumed a planar adsorption geometry at this minimum, on both substrates. In this planar orientation, on the basis of van der Waals interactions only, we would expect the binding of G to be stronger than that of A (due to the presence of the carbonyl group on G, which is not featured in A). This is in fact the case for the C(0001) surface. However, our previous work indicates that the unprotonated nitrogen site (as found in the aromatic ring for both dA and dG) favors a strong interaction with the Au surface, even under aqueous conditions.⁶ This interaction between the unprotonated nitrogen site on the ring can give rise to an adsorption geometry where the ring is oriented perpendicular to the surface (see **Figure B.1.4**). This type of interaction is not supported at the C(0001) interface. Furthermore, we propose that steric hindrance (due to the presence of the carbonyl group on dG, which is not featured in dA) hindered this perpendicular adsorption geometry for dG, but not for dA. This additional adsorption geometry, present only for dA on Au(111), was also evident in the FE profiles of A and G adsorbed at the Au(111) interface. These profiles reveal an additional local minimum in the FE profile for A, located $\sim 6 \text{ \AA}$ from the Au surface, corresponding with this perpendicular geometry. *Via* our integration of the FE profiles, this

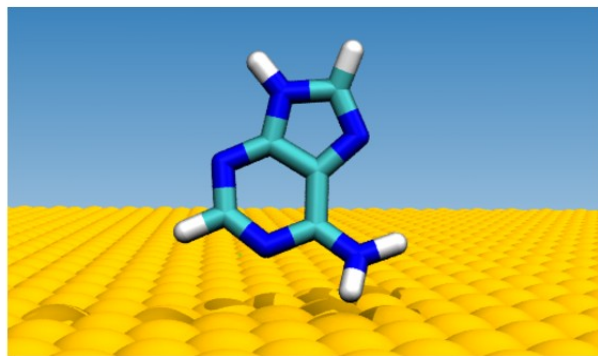


Figure B.1.4. Snapshot of the perpendicular adsorption geometry of the adenine nucleobase, which is not supported by guanine (see text for details). Water not shown for clarity.

additional minimum in the FE profile for the adenosine nucleobase contributes to the stronger binding affinity of A at the Au(111) interface compared with G. As far as the absolute values of the adsorption free energy are concerned, for all four bases on both substrates the metadynamics simulations showed a progressive increase from the nucleobase to the nucleoside to the nucleotide (**Table B.1.1**). However, these data also indicate that the presence of the deoxyribose and phosphate groups appeared in general to reduce the relative differences between the different bases.

Conclusions. In conclusion, our combined experimental and modeling approach, in partnership with careful analysis, provides a valuable and versatile strategy for quantifying and interpreting the binding traits of nucleic acid/materials interfaces. In the present work, the binding strengths of nucleic acid fragments on aqueous C(0001) and Au(111) determined experimentally by our collaborators using single molecule force spectroscopy measurements were predicted *via* our all-atom metadynamics simulations based on polarizable force-fields. We found reasonable consistency between the experimental and modeling data. However, the consideration of several limitations and approximations, inherent to both the experimental interpretation of the adhesion force data and the calculation of the metadynamics-based free energies, hindered a clear-cut comparison of relative binding strengths, particularly for the Au substrate. On C(0001), our simulations predicted a binding trend of $dG > dA \approx dT > dC$, which was broadly consistent with the experimental data. At the aqueous Au(111) interface, the relative binding strength of adenine was significantly increased, a fact that we could rationalize *via* analysis of the binding conformations predicted by the simulations. This led to a slightly different adsorption trend on Au(111), namely $dG \approx dA > dT \approx dC$. In agreement with several previous studies, our simulations suggested little to no influence of salt concentration on the predicted binding strengths. Our modeling data also provided insights into the adsorption geometries at these substrates, as a function of nucleic acid fragment size, by considering binding of the nucleobases, nucleosides and nucleotides. In general, the binding trends predicted for both substrates was consistent across these three levels of fragment size.

B.2. Structural disruption of an adenosine-binding DNA aptamer adsorbed on graphene

In many aptasensor applications, integration of the aptamer with a surface/substrate is a necessary requirement. One substrate that is particularly promising is graphene, with its many desirable properties such as conductivity, flexibility and transparency. However, to advance the development of aptamer/graphene-based sensing platforms, a well-developed understanding of the how the molecular structure of the aptamer may be affected by the presence of the substrate, in the presence and the absence of the target analyte, is needed. In particular, the question of whether the substrate might degrade the aptamer structure and possibly reduce the aptamer binding affinity and/or selectivity is critical.

Considering the aromatic character of both the nucleobases and graphitic substrates, it is not surprising that previous studies indicate a strongly favorable interaction between the two. However, despite the strong favorable interaction with graphene at the nucleobase level, the greater macromolecular structure of an oligonucleotide structure may play a pivotal role in governing how the aptamer interaction with the aqueous graphitic interface. This phenomenon may for example result in the different behavior reported for the interaction of ssDNA and dsDNA with solid surfaces. Overall, the interaction of oligonucleotides with graphitic substrates therefore depends on the balance between nucleotide base pairing, nucleotide π - π interactions, backbone flexibility and nucleotide-substrate π - π interactions. In many instances, DNA aptamers may contain both regions of dsDNA and ssDNA, and therefore the molecular-scale details of the aptamer-graphene interaction may depend strongly on the nature of the aptamer.

The DNA aptamer ACCTGGGGGAGTATTGCGGAGGAAGGT has been shown to bind adenosine, adenosine triphosphate (ATP) and adenosine monophosphate (AMP) at micromolar concentrations. The ability to detect small variations in AMP levels under physiological conditions is highly relevant to a range of health conditions, including diabetes and obesity. The three-dimensional solution structure of this aptamer when complexed with two adenosine molecules (herein referred to as the *holo* form) has been reported based on nuclear magnetic resonance (NMR) spectroscopy studies (PDB-ID:1AW4).⁷ Four Watson-Crick (WC) base pairs are present in the duplexed stem of aptamer, followed by a guanine rich region containing two non-equivalent ligand binding pockets, located at G9 and G22, and then finally two more base pairs (one WC, one mismatch) and a small trimeric loop (A13-T14-T15) at the distal end of the aptamer. While the structure of the *holo* form is well characterized, there are still some questions over the degree of conformational change in the absence of the analyte. Previous NMR studies suggested only minor conformational changes upon ligand binding,⁷ a conclusion supported by quartz-crystal microbalance (QCM) experiments of biotinylated aptamers deposited on a sensors. However, this finding may not be consistent with single-pair Förster resonance energy transfer (spFRET) spectroscopy measurements that indicate the ligand-free form (herein referred to as the *apo* form) resembles that of the *holo* form under high salt concentrations, while suggesting that at low salt concentrations the *apo* aptamer is more dynamic, preferring an unfolded conformation. Moreover, very recent studies indicate that the binding of the target into the two binding pockets is only weakly co-operative, with single-pocket variants of this aptamer binding with similarly high binding affinity and specificity.⁸

Recently, the use of this aptamer, *via* physical adsorption onto graphene substrates, has yielded a successful demonstration of a proof-of-concept field-effect-transistor (FET)-like electromechanical biosensor device for the detection of ultra-low concentrations of AMP.⁹ However, in this device the authors used a pyrene tag placed at the 5' end, which may have influenced the adenosine capabilities of the aptamer. Despite this encouraging progress, the systematic improvement of such devices hinges on our ability to monitor, elucidate, and manipulate the structure of such aptamers when adsorbed at the graphene interface. However, the task of clearly elucidating the molecular-level structure(s) of biomolecules adsorbed to solid surfaces under aqueous conditions remains a challenging task. Therefore, in comparison with the current uncertainty regarding the molecular-level of the structure of the *apo* form, it is likely that an even greater degree of uncertainty may hinder our ability to determine these surface-adsorbed aptamer structures.

Fluorescent measurements of the aptamer physisorbed to the aqueous graphene oxide interface showed that this aptamer retained selective binding of ATP, but also suggested a degree of conformational change in the molecule. Recent experimental efforts based on atomic force microscopy (AFM), namely single molecule force spectroscopy (SMFS) investigated the interaction of this aptamer with the aqueous graphite interface.¹⁰ These SMFS experiments showed that by pulling the surface-adsorbed aptamer from aqueous graphite interface this produced a stable force plateau in the measured force-distance curves, which can be interpreted as representing the successive, base-by-base desorption of the strand from the surface. Moreover, SMFS measurements of dsDNA at aqueous graphite interfaces reported a relatively reduced level of force required to remove the molecule from the substrate. It may be viewed as perhaps counter-intuitive that the peeling force required to pull the aptamer from the aqueous graphite interface was ~ 40 % higher in the presence of adenosine

compared with that measured in the absence of adenosine. These data suggest that the *holo* form interacted more strongly with the substrate than the *apo* form.

With the challenge of obtaining experimental structural data at the relevant length-scale for these surface-adsorbed aptamers, under aqueous conditions, MD simulations comprise an alternative that can provide complementary information. Relatively few simulation studies have been published to date regarding aptamer adsorption at aqueous/solid interfaces, but there is a significant body of work

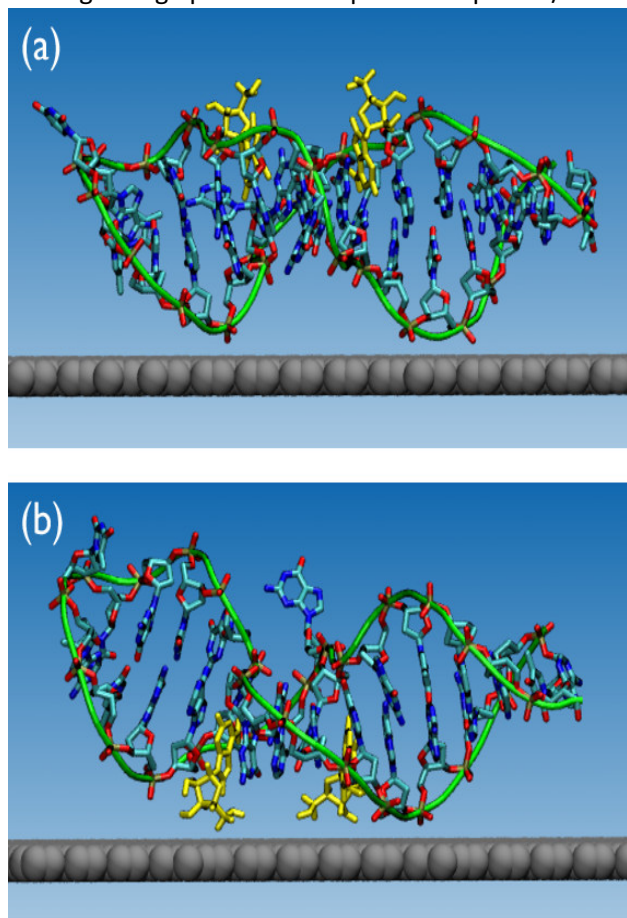


Figure B.2.1. Snapshots showing the (a) Up and (b) Down orientations. Water molecules and hydrogen atoms are not shown for clarity. Color code: adenosine molecules in yellow, graphene surface in grey, aptamer backbone in green, while the carbon, nitrogen and oxygen atoms of the aptamer are colored cyan, blue and red, respectively.

on the interaction of DNA/RNA oligomers at the aqueous/ solid interfaces for substrates such as gold, graphene and/or CNTs and others. As mentioned earlier, MD simulations have suggested very different adsorption modes for ssDNA compared with dsDNA at graphene interfaces, with dsDNA thought to undergo far less conformational change upon adsorption.

Here, we have used MD simulations to investigate the structure of a DNA aptamer, both in the *apo* and *holo* forms, both free in solution and when adsorbed at the aqueous graphene interface. In the absence of the surface, we found that both forms possessed a strong degree of secondary structure, and that the structure of the aptamer did not unravel completely in the *apo* form. When adsorbed at the graphene interface, a variety of different adsorbed configurations were predicted. The purpose of this work is two-fold. First, we wanted to check our ability to use MD simulations to recover the structure of this aptamer, given that a clear NMR-based structure is publicly available for comparison. Our second aim was to investigate the basis for the intriguing results reported by recent SMFS experiments on this system, as summarized above.

Methodology. The DNA aptamer and adenosine molecules were described using the CHARMM27 forcefield (FF), with the modified TIP3P model used to represent water molecules. The interactions of water and aptamers with the graphene interface was described using the the polarizable GRAPPA FF.

The initial structure of the 1AW4 aptamer was taken from the protein database (PDB-ID: 1AW4). The *apo* and *holo* forms of the aptamer were simulated in bulk solution and at the aqueous graphene interface. In all cases the aptamer was simulated in 0.05 mol kg^{-1} NaCl (the same salt concentration used for the SMFS measurements of the molecule). The bulk solution simulations consisted of the aptamer, and in the *holo* form, two adenosine molecules, and ~ 23800 water molecules in a

$\sim 89.4 \times 89.4 \times 89.4 \text{ \AA}^3$ simulation cell. The surface-adsorbed simulations systems comprised the aptamer (and in the *holo* form, two adenosine molecules) and ~ 23800 water molecules in the presence of a graphene sheet $\sim 88.5 \times 89.5 \text{ \AA}^2$, with a 93.5 \AA distance separating the sheet from its periodic image along the cell direction perpendicular to the graphene surface plane. Other simulation details follow those reported in **Section B.1**. Two independent 250 ns simulations were performed for each form (*apo* and *holo*) in bulk solution. For the adsorbed systems, each form was simulated starting from two different initial orientations: **Up**, where the binding pockets were directed away from the graphene surface and exposed to the bulk solution, and **Down**, where the binding pockets (plus adenosine molecules in the *holo* form) were directed towards the graphene sheet, as shown in **Figure B.2.1**. For each system (*apo* up, *apo* down, *holo* up, *holo* down) two independent 300 ns simulations were performed. Both the initial velocities and initial coordinates were different for every simulation run.

We anticipate that the aptamer will feature a complex potential energy landscape, particularly in the surface-adsorbed state, which means that even 250/300 ns may not be sufficient to ensure that the system does not become trapped in high-energy (metastable) minima. As such, in addition to performing the above simulations at 300 K, a further set of simulations was also performed, where after 100 ns (50 ns for the solution systems) at 300 K, the system was subjected to a series of simulated annealing (SA) cycles. Each SA cycle consisted of heating the system from 300 to 400 K over 0.5 ns, 2 ns at 400 K and a 2.5 ns period where the system was cooled from 400 back to 300 K. During the SA cycle the volume of the system was kept constant. Each surface-adsorbed and bulk solution simulation was subjected to 10 and 5 SA cycles, respectively. At the conclusion of these SA cycles, the adsorbed/solution systems were subjected to a further 150/175 ns of simulation at 300 K, respectively.

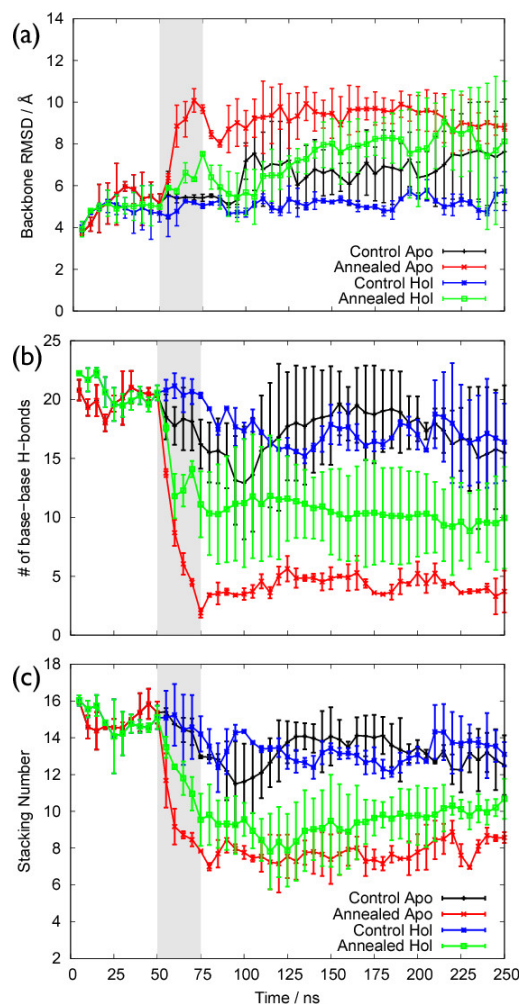


Figure B.2.2. Data for DNA aptamer in solution, averaged over two runs for each system: (a) the RMSD of the aptamer backbone atoms, (b) the number of DNA nucleobase-nucleobase hydrogen bonds and (c) the base stacking number as a function of simulation time. The shaded area indicates the period where the simulated annealing protocol was applied to the annealed runs.

Results and Discussion.

Simulations of the Aptamer in Solution. Figure B.2.2 summarizes the MD simulation results for different bulk solution systems, averaged over the two runs, for each system. Even after 250 ns of MD simulation the control runs of both the *holo* and the *apo* forms revealed only minor differences compared with the initial aptamer structure. The backbone RMSD of the *holo* form did not vary significantly over the course of the control runs, and that of the *apo* form showed only a minor increase in backbone RMSD. Similarly, the number of nucleobase-nucleobase hydrogen bonds and the stacking number were broadly unchanged. Application of the SA procedure to the DNA yielded more substantial changes to the base-base interactions of the aptamer, with a reduction in the number of stacked bases and the number of base-base hydrogen bonds, especially for the *apo* form. In turn, this disruption to the intra-molecular interactions facilitated a greater degree of change to the aptamer backbone structure compared with the control runs. That said, the final structures of the aptamer still resembled those of the initial aptamer structure quite closely, as shown in Figure B.2.3.

For the control runs all four of the adenosine molecules remained bound to the aptamer over the course of the simulations. For the SA runs, one adenosine molecule (out of the four) escaped the binding pocket of the aptamer. However, in this instance the adenosine still remained bound to the aptamer (on the exterior of the binding pocket), suggesting that the SA procedure did not disrupt the aptamer to such an extent so as to expel the bound ligands.

Overall, these data indicate that structure of the aptamer in solution is highly stable, and even when exposed to the SA procedure maintained a strong structural integrity. These results are also consistent with the majority of experimental evidence, with the consensus view that the conformation of the *apo* form remained folded and resembled the *holo* form.

Simulations of the Adsorbed Aptamer. Figure B.2.4 shows the number of nucleobases adsorbed to the aqueous graphene interface as a function of simulation time for the control simulation runs. The nucleobases adsorbed in a stepwise fashion, as is characteristic of adsorption of nucleobases at graphitic surfaces, with very few nucleobase desorption events noted here. After 300 ns of control simulation, most systems featured only a relatively small proportion of adsorbed bases, between 7-5-%. However, there was a substantial degree of variation in this metric, even between runs of the same system, making it challenging to conclusively determine any effect of initial orientation (up or down) or form (*i.e.* *apo* or *holo*), although there is some suggestion that a greater number of bases might be adsorbed for the *holo* form. Subjecting the aptamer to the SA process disrupted the internal structure of molecule and thus encouraged further adsorption of the nucleobases, as shown in Figure B.2.5. While the annealing simulations did not show any significant effect of initial

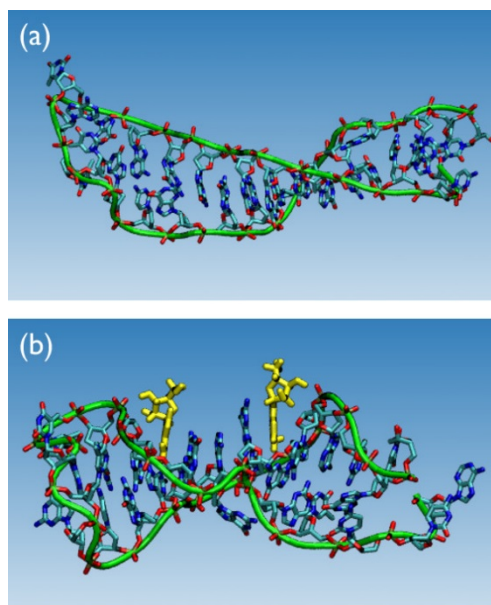


Figure B.2.3. Snapshots of representative aptamer configurations in bulk solution for (a) the *apo* and (b) the *holo* form annealing runs. Water molecules and hydrogen atoms in the aptamer are not shown for clarity. Color code: adenosine in yellow, aptamer backbone in green, while the carbon, nitrogen and oxygen atoms of the aptamer are colored cyan, blue and red, respectively.

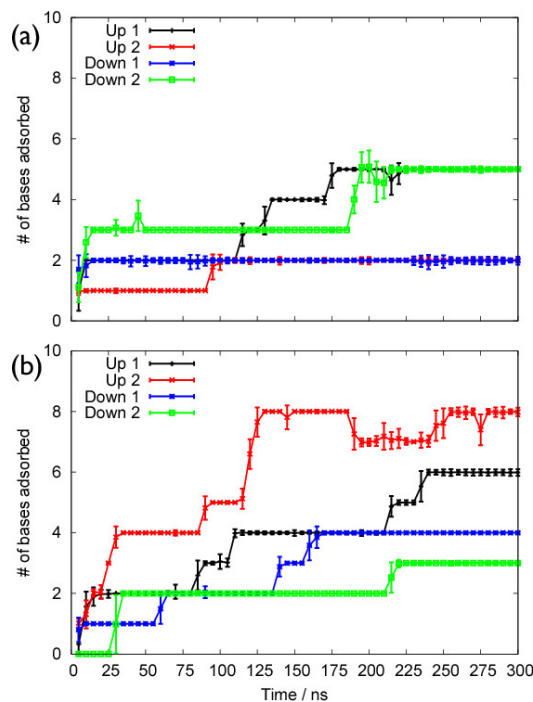


Figure B.2.4. The number of nucleobases directly adsorbed to the graphene surface in the control simulations for (a) the apo and (b) the holo forms of the aptamer.

orientation (up or down) for the *holo* form, there is a distinction for the *apo* form, where the Down orientation produced a greater number of adsorbed bases. Over the four runs, the *holo* form yielded a greater number of adsorbed bases compared with the *apo* form (29 vs. 25 bases). However, the variance between individual runs was still too great to conclusively demonstrate that this result is statistically significant.

As mentioned earlier, previously reported simulations of DNA adsorbed at aqueous graphene interfaces have shown that ssDNA and dsDNA support different adsorption modes, with ssDNA typically featuring a large proportion of nucleobases directly adsorbed on the surface, while dsDNA is often reported as adsorbed to these substrates either indirectly, or directly only *via* the terminal bases. In general, an aptamer might be expected to support a mixture of both types of binding modality, because aptamers tend to feature regions of both ssDNA and duplex characteristics. To elaborate, while there are typically regions of strong intra-base interaction in a given aptamer, there may also be ssDNA-like regions, such as the analyte binding site, where surface adsorption may be likely.

In addition to the bases in the vicinity of the binding pocket, other regions in this aptamer may also be susceptible to adsorption at the graphite surface. These regions include the terminal pair of nucleobases at the open end of the stem (A1 and T27) and the bases in the small loop at the distal end of the aptamer (A13-T14-T15). In fact, nucleobases from all three of these locations within the aptamer adsorbed at the graphene interface, although each individual simulation may only support adsorption at one or two of these locations. **Figure B.2.6** provides snapshots of the final configurations from different simulations, illustrating the variety of different binding modes that the aptamer supported when adsorbed at the aqueous graphene interface. These snapshots include conformations with only the terminal nucleobases (A1 and T27) bound to the surface (where the long axis of the aptamer is approximately perpendicular to the surface plane (**Figure B.2.6(a)**), conformations where the aptamer is adsorbed in a parallel fashion (**Figure B.2.6(b) and (d)**) and geometries where direct surface contact is primarily mediated *via* the bases in the binding pocket (**Figure B.2.6(c)**).

The data illustrated in **Figure B.2.5**, offers a possible explanation for the differences observed between the Up and Down orientations of the *apo* form. For the simulations started in Up orientation, the adsorbed nucleobases were chiefly located in the head and tail regions of the aptamer. In contrast, for the simulations started in the Down orientation, a large proportion of the adsorbed bases were located in the central region of the aptamer corresponding with the position of the binding pockets. This is understandable because the simulations started in the Down orientation positioned the binding pocket directed towards the graphene surface, while in the Up orientation the center of the aptamer was instead exposed to the solution (see **Figure B.2.1**). In the case of the *holo* form in the Down orientation, we propose that the presence of the adenosine molecules may hinder the adsorption of nucleobases in this location, even if in some instances the adenosine molecules escaped from the aptamer pocket (see below).

For the control simulations started from the Up orientation, none of the four adenosine molecules (two per aptamer, over two simulations) became unbound. However, for the simulations started from the Down orientation, one adenosine molecule in one run become unbound and instead

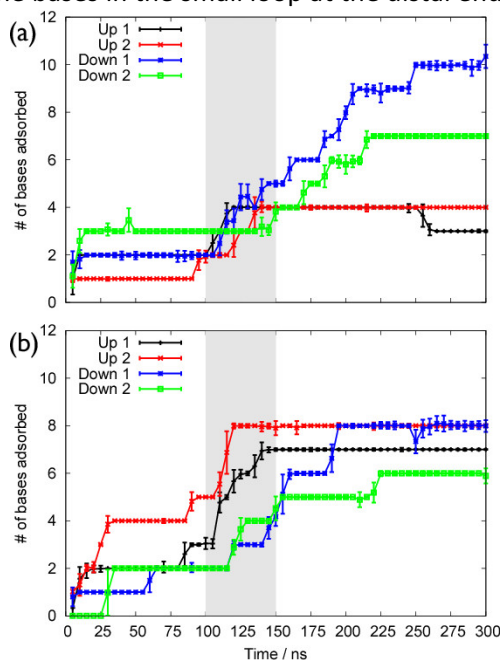


Figure B.2.5. The number of nucleobases directly adsorbed to the graphene surface in the annealing simulations as a function of simulation time for (a) the apo, and (b) the holo forms of the aptamer.

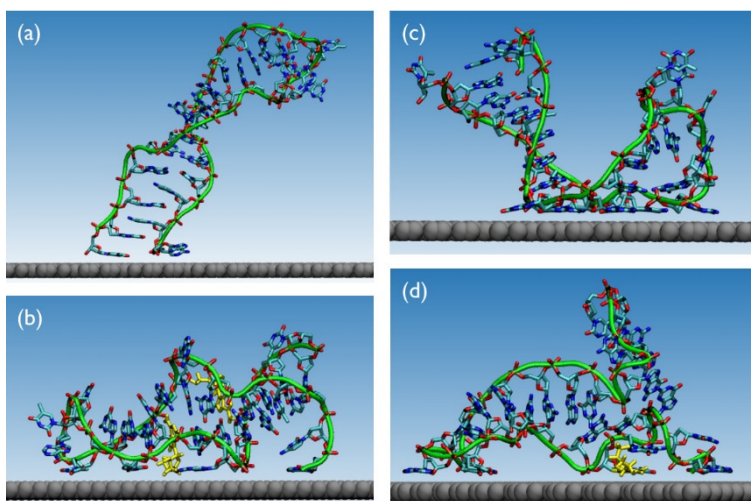


Figure B.2.6. Snapshots of representative configurations of (a,c) the apo and (b,d) the holo forms from the control (a,b) and annealing (c,d) simulations. Snapshots were taken from simulations starting in the Down configuration. Water molecules and hydrogen atoms in the aptamer are not shown for clarity. Color code: graphene surface in grey, adenosine molecules in yellow, aptamer backbone in green, while the carbon, nitrogen and oxygen atoms of the aptamer are coloured cyan, blue and red, respectively.

become bound to the graphene surface. For the annealing runs, both ligands were expelled from the binding pocket in all but one run (in the Up orientation). After detaching from the binding pocket, the adenosine molecules quickly (and on the timescales of the simulations irreversibly) adsorbed to the graphene surface, and typically interacted with adsorbed bases of the aptamer. In summary, these simulations suggest that the adsorption of the aptamer to the aqueous graphene interface might interfere with the binding of the analyte in the binding pocket, particularly if the molecule is adsorbed in a Down orientation.

The variation of the backbone RMSD, number of intra-base H-bonds and base stacking number for all the simulation runs of the surface-adsorbed systems (averaged over all four runs for each system) are shown **Figure B.2.7**. As already noted for the aptamer in bulk solution, the control simulations of the adsorbed aptamer showed only minor variation in these metrics over the 300 ns duration, with the *apo* showing a small, but statistically significant increase in RMSD and decrease in the number of base-base hydrogen bonds. The SA procedure induced a similar disruption to the intra-molecular structure of the aptamer, as also seen for the aptamer in bulk solution, captured by a decrease in the intra-base hydrogen bonding and base stacking number, along with an increase in the backbone RMSD. The large differences between runs have resulted in large calculated uncertainties, but on average the backbone RMSD was greater for the *apo* form than the *holo* form. Comparing the results of the surface-adsorbed systems against the aptamer free in bulk solution, no statistically significant differences are observed,

confirming that even in the adsorbed state substantial intra-molecular interactions were present in this aptamer.

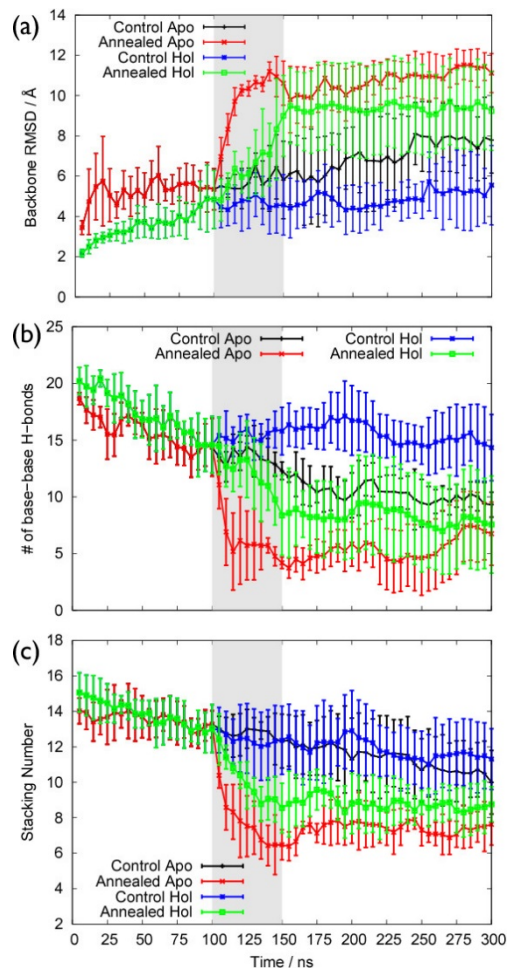


Figure B.2.7. Results of simulations of the DNA aptamer adsorbed at the aqueous graphene interface, averaged over four runs for each system: (a) the RMSD of the backbone atoms of the aptamer, (b) the number of DNA nucleobase-nucleobase hydrogen bonds and (c) the base stacking number as a function of simulation time. The shaded area shows the period where the simulated annealing protocol was applied to the annealed runs.

As mentioned earlier, previous SMFS experiments reported that a greater force was required to detach the aptamer from the aqueous graphene interface after the addition of adenosine, compared with the peeling force of the surface-adsorbed aptamer in the absence of adenosine.¹⁰ Moreover, this effect was only observed for adenosine, *i.e.* the addition of other nucleosides did not lead to any increase in the peeling force. Li *et al.* explained this by proposing the *apo* form would follow a ssDNA-like adsorption mode, with most of the bases in direct contact with the graphene substrate, such that the bases would successively desorb (one by one) when subjected to the peeling force. Furthermore, these authors also hypothesized that, in the *holo* form (in the presence of adenosine) the presence of the adenosines in the binding pockets may hinder this successive, base-by-base detachment process, and therefore would require a greater force to desorb the aptamer from the surface.

In contrast with this hypothesis from Li *et al.*,¹⁰ the results of our simulations suggest that even the *apo* form retained a substantial amount of secondary structure when adsorbed at the aqueous graphene interface. In this case, more than half of the bases were not directly bound to the surface. However, one complication in comparing our simulations with the current experimental data is the role of adenosine (or the other nucleosides that were added in the control experiments). To elaborate, in the SMFS experiments the sample cell was first filled with the analyte solution, and following this the aptamer-functionalized AFM probe was submerged in this solution for 1 hour, prior to being lowered into contact with the graphite (HOPG) substrate. Our simulation results suggest that the graphite substrate could compete with the aptamer for the binding of the adenosine molecules present in the solution.

Both simulation and experiment suggest that adenosine binds strongly at the aqueous graphene interface (summarized in **Section B1**). This binding strength, ranging from -41 to -24 kJ mol^{-1} , is competitive with (or exceeds) the experimentally-determined adenosine-aptamer binding strength of -27 kJ mol^{-1} . However, aptamers that target analytes other than adenosine may quite likely face less competition from the graphene substrate. Therefore, it is possible in these experiments that the nucleosides in the solution adsorbed to the HOPG substrate prior to the aptamer binding event, and these pre-adsorbed nucleosides might have interacted with the nucleobases in the aptamer. In fact,

previous simulations have shown that nucleobase dimers adsorbed at aqueous graphene interfaces can be stabilized *via* hydrogen bonding (both WC and non-WC). Therefore, the force required to desorb the aptamer in the presence of adenosine may be due to the presence of substrate-bound adenosine molecules, which could conceivably strengthen the interaction of aptamer with the substrate. However, how and why such an effect is not observed in the presence of other nucleosides in solution is a question that requires further investigation, both experimental and modeling, to address.

Conclusions. We used molecular dynamics simulations to predict the structure and properties of the adenosine-binding DNA aptamer in the presence and absence of the target analyte, both when free in bulk solution, and when adsorbed at the aqueous graphene interface. Our simulation results indicate that graphene adsorption can support a variety of different binding modes, with both the terminal bases, the loop, and binding pockets susceptible to surface adsorption. However, the maximum number of adsorbed nucleobases did not exceed ten (37%), which is a smaller proportion of adsorbed bases than has been typically reported observed in simulations of unstructured ssDNA adsorbed at graphene interfaces. In addition, the strong intra-molecular interactions present in the aptamer competed with the graphene-aptamer interactions, as has been previously reported for simulations of duplex DNA adsorption. Therefore, this aptamer exhibited a mixture of ssDNA-like and dsDNA-like adsorption modes, with substantial retention of intra-molecular interactions. However, our simulations suggest that the binding affinity and selectivity of adenosine in some instances may be affected by the presence of the aqueous graphene interface. For some of the favorable adsorbed configurations predicted by our simulations, detachment of the adenosine analytes may have been facilitated by competition between adenosine-pocket and adenosine-graphene interactions. However, adenosine is thought to bind strongly at aqueous graphitic substrates, and therefore aptamers that target analytes other than adenosine may quite likely face less competition from the graphene substrate. Overall, our simulations indicate that while DNA aptamer-based devices have considerable potential, the balance of competitive interactions amongst the aptamer, the target analyte, and the substrate must be considered. Molecular dynamics simulations can provide valuable insights into this balance and therefore the choice and suitability of a device substrate with a given aptamer.

B.3. Structural predictions of the MN4 aptamer in the presence and absence of cocaine

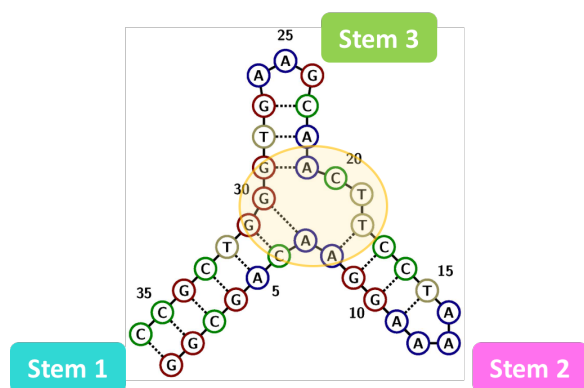


Figure B.3.1. Proposed three-stem structure of MN4 in the absence of cocaine, suggested by Neves *et al.*² Yellow shading indicates the putative cocaine binding site.

Recent NMR and binding assay studies conducted at AFRL (Mirau *et al.* Ref 3) have investigated the 36-nucleotide (36-nt) cocaine-binding aptamer, commonly referred to as MN4, adsorbed at the aqueous Au NP surface. Their findings indirectly indicate the loss of nucleotide pairing in the absence of the cocaine analyte.

While the 3-D atomic-scale structure of the MN4 aptamer has not yet been published, previously-reported NMR data¹¹ are consistent with the proposed three-stem structure illustrated in **Figure B.3.1**. Because the 3D atomic coordinates for MN4 are

currently unavailable, our first task in this phase of the project was to build, predict, verify and refine this structural model of MN4 in solution (in the absence of Au nanoparticles, NPs). We predicted and characterized the structure of MN4 in solution in both the presence and absence of cocaine. Previous NMR studies [Refs 2,3] suggest that the central three-stem junction is the likely binding site for cocaine, consistent with the formation of a 1:1 complex.

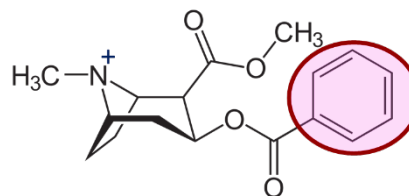


Figure B.3.2 Molecular structure of cocaine. The pink shading indicates the aromatic head region.

Cocaine comprises a bulky non-aromatic tail region that is capable of acting as both a hydrogen bond donor and acceptor, and a phenyl-based aromatic head region (**Figure B.3.2**). The nitrogen site in the tail region is thought to be positively charged under aqueous conditions and neutral pH.

Methodology

Generation of the initial aptamer coordinates: We used *de novo* prediction software, WC-Fold, to generate a guideline on the 3-D coordinates for the MN4 structure. However, WC-Fold is configured to provide 3D coordinates of RNA structures only. Therefore, we converted the output of the WC-Fold prediction into a DNA-appropriate form.

Simulation details: We used these initial coordinates as input for molecular dynamics (MD) simulations using the GROMACS v 5.0.x software package. In these simulations, we modeled liquid water at the

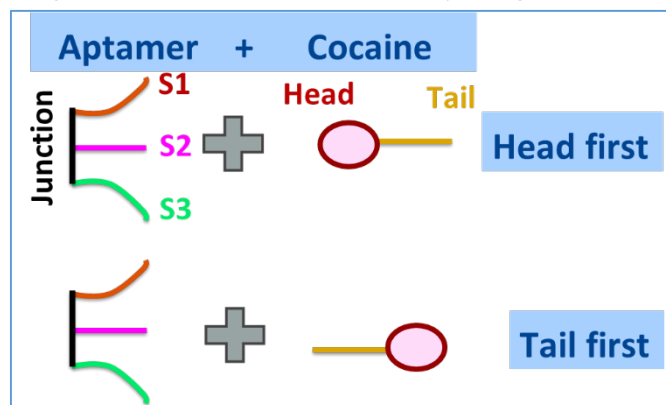


Figure B.1.3. Illustration of the two types of initial geometry for the aptamer-cocaine simulations. The MN4 aptamer is depicted with three stems (S1-S3) and a junction. The cocaine was placed into the central junction of MN4 either head first, or tail first.

molecular level using the SPC water force-field (FF), while the aptamer was described using the AMBER ff99 force-field. The structure of the cocaine molecule was built by hand. The force-field used to describe the cocaine interactions with the water, salt and aptamer was provided by Zhan and co-workers, and designed to work in harmonization with the AMBER DNA force-field. Counter-ions (to balance the negative charge of the aptamer), in the form Na^+ , were added to the system, and their interaction with water and DNA was captured using the revised Dang Na^+ parameters. Additional Na^+ and Cl^- ions were then added to the

simulation cell to ensure that the resulting NaCl solution had a concentration of 25 mM. A range of salt concentrations was explored initially, before settling on the use of the 25 mM concentration. The number of water molecules in the cell was around 107,000 (in a periodic cell of dimensions $\sim 150 \times 150 \times 150 \text{ \AA}^3$). The aptamer-only MD simulation cell comprised a single copy of the MN4 aptamer, liquid water, and ions as described above. The aptamer-cocaine simulation cell comprised one MN4 aptamer, one cocaine molecule, liquid water, and ions as described above.

Each MD simulation was run for a duration of 300 ns in the isothermal-isobaric ensemble (NPT ensemble) at ambient temperature (300 K) and pressure (1 atm). For the aptamer-only simulations, we ran our MD simulations in triplicate (three independent simulations). For the aptamer-cocaine

simulations, we ran six independent simulations. To elaborate, we used two types of initial geometry for the aptamer-cocaine simulations, which were distinguished on the basis of the initial orientation of the cocaine adsorbate relative to the aptamer, as illustrated in **Figure B.3.3.**, as either “head-first” or “tail-first”. This was done to ensure our simulation outcomes were not biased by our choice of initial aptamer-cocaine geometry. We performed three independent simulations of both the head-first and tail-first geometries.

Results and Discussion

Our predicted structure of the MN4 aptamer (**Figure B.3.4**) in the absence of cocaine is broadly consistent the structures been proposed in the literature previously. Our simulations yielded a 3D structure with three duplexed stems and a central junction region that featured very few signs of conventional Watson-Crick base pair interactions. Based on the proposed NMR structure (**Figure B.3.1**) we would expect to see substantial hydrogen bonding between six base pairs in **Stem 1**: G1-C36, G2-C35, C3-G34, G4-C33, A5-T32, and C6-G31. Neves *et al.* also proposed a tentative assignment of a non-conventional base-pair between A7 and G30. Similarly, based on Neves *et al.*'s work, in **Stem 2** we expected the following base-pairings: A8-T18, G9-C17, G10-C16, and A11-T15, whereas in **Stem 3** we expect base-pair hydrogen bonds between A22-T28 and C23-G27. Neves *et al.* tentatively proposed an additional non-conventional hydrogen-bonded interaction between A21 and G29. The two experimentally-proposed non-conventional base-pairings (A7-G30 and A21-G29) are indicated with dashed lines in **Figure B.3.1**, and are proposed to be positioned next to each other in a tandem arrangement.

Based on our three independent simulations of cocaine-free MN4 in solution, we predicted the average likelihood of finding at least one hydrogen-bond between each pair of all possible base pairs, as summarized in **Figure B.3.5**. As expected, we found strong Watson-Crick hydrogen-bonded contact in Stem 1 base pairs G2-C35, C3-G34, G4-C33, A5-T32 and C6-G31. Likewise we found similar strong contact in Stem 2 base pairs A8-T18, G9-C17, G10-C16, and A11-T15, and Stem 3 base pairs A22-T28 and C23-G27. However, our predictions deviate slightly from Neves *et al.*, as illustrated in **Figure B.3.5** First, no hydrogen bonding was found between Stem 1 base pairs G1-C36. This was due to the conformational

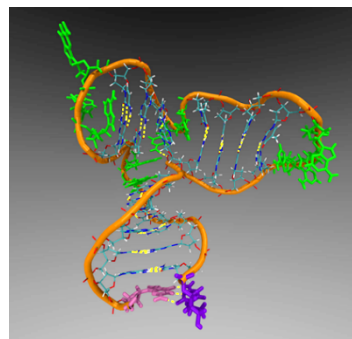


Figure B.3.4. Snapshot of the predicted structure of the cocaine-free MN4 aptamer in solution. Water and ions not shown for clarity. Yellow dotted lines indicate base-base hydrogen bonds. Green coloring highlights un-paired bases. The pink and purple colors indicate the 3' and 5' ends of the chain.

freedom experienced by these 3' and 5' nucleotides (NTs), which led to fraying of the open duplex end. This behaviour is entirely consistent with our previous structural predictions of aptamer structures based on MD simulation in liquid water at room temperature.

Second, we did not observe the tandem pair of unconventional G---A base pairings (A7-G30 and A21-G29) suggested by Neves *et al.* While we did predict a modest (< 30%) likelihood of occurrence of the A7-G30 base pair, we found no evidence of a A21-G29 pairing. Instead, we predicted a modest (< 30%) likelihood of three other unconventional pairings that are similarly positioned nearby to the A7-G30 base pair in the central junction, namely A7-T19, C20-G29, and (with <10% likelihood) A7-A21.

In summary, our simulations of cocaine-free MN4 yielded an approximately umbrella-shaped three-stem aptamer structure, with a central stem junction featuring a number of bases that do not extensively participate in base pairing, principally A7, T19, C20, A21, G29 and G30. These bases are anticipated to be likely sites for cocaine interaction, due to their availability.

Our simulations of the MN4-cocaine complex suggested that this complex is structurally stable, at least over the timescale of our simulations (300 ns), with no suggestion of incipient destabilization as a function of simulation time. Specifically, our head-first initial conformations remained in a head-first arrangement, whereas one of our simulations initiated in the tail-first configuration rearranged into an intercalated configuration. Exemplar images of the three types of structures are provided in **Figure B.3.6**. The majority of the simulations resulted with the cocaine remaining in the head-first position.

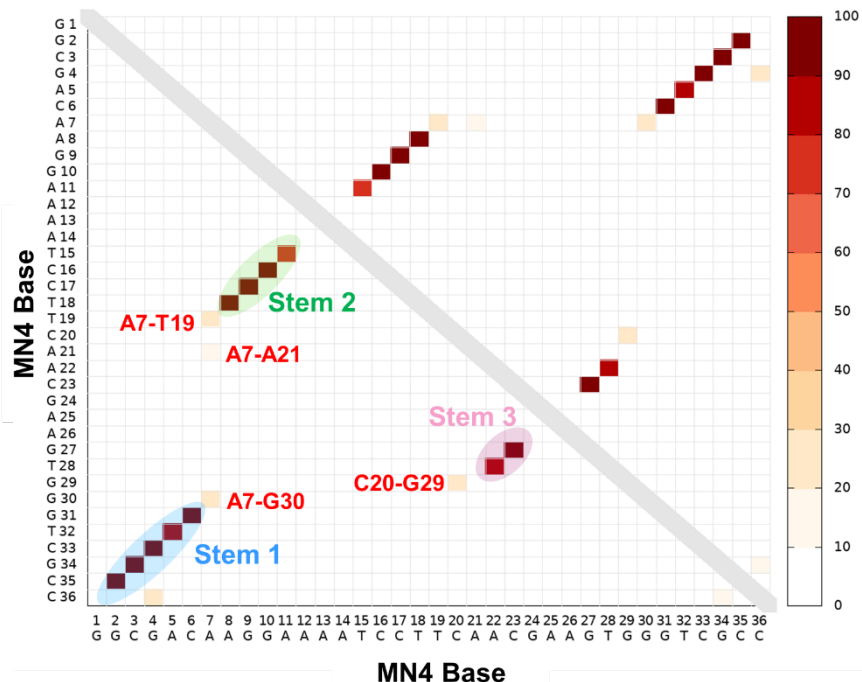


Figure B.1.5. Predicted map of hydrogen bonds between bases in the MN4 aptamer in the absence of cocaine. Color-scheme indicates the average likelihood of at least one hydrogen bond to be present between a given pair of bases, where 100% = always present, 0% = never present. The hydrogen bonding patterns associated with Stems 1-3 are indicated with colored ellipses, consistent with duplex DNA in these regions. Non-stem base pair hydrogen bonds are highlighted in red text and indicate intermittent contact in the junction region.

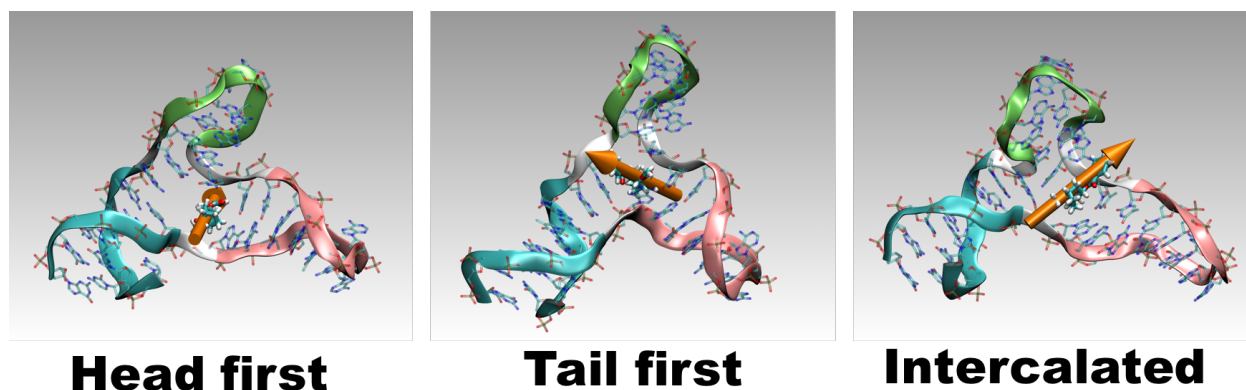


Figure B.3.6. Exemplar snapshots of the MN4-cocaine complex predicted using molecular dynamics simulations. Water and ions not shown for clarity. Stems 1, 2 and 3 are colored blue, pink and green respectively. The cocaine analyte is rendered in thicker bonds. The orange arrow indicates the orientation of the cocaine molecule.

Our collaborator (Bedford, AFRL and UNSW) used SAXS observations to probe if the binding of cocaine induced a broad change in the conformation of MN4. The radius of gyration, R_g , of cocaine-free and cocaine-bound MN4 was inferred from these SAXS data. Dr. Bedford's reported R_g values for the cocaine-free and cocaine-bound MN4 were $14.4 \pm 0.5 \text{ \AA}$ and $17.6 \pm 0.3 \text{ \AA}$ respectively. These SAXS data suggest that the aptamer undergoes a small conformational change when it binds cocaine, such that the spatial extent of MN4 slightly increases relative to MN4 in the cocaine-bound state. To make a like-for-like comparison, we calculated the average R_g from our MD simulation data, and predicted R_g values for the cocaine-free and cocaine-bound MN4 of $15.6 \pm 0.3 \text{ \AA}$ and $17.2 \pm 0.3 \text{ \AA}$ respectively. Therefore, our MD simulations are consistent with the findings from the SAXS experiments. To further explore how MN4 enhances its spatial extent, we searched for additional metrics to quantify the cocaine-induced conformational change. From visual inspection of the MD simulation trajectories, we noticed that the 3D umbrella-like conformation of MN4 flattened somewhat when the cocaine was bound to the central junction, as illustrated in **Figure B.3.7**. To capture this "flattening" conformational transition, we calculated the longest point-to-point distance, d , in the molecule for both the cocaine-free and cocaine-bound states of MN4. In physical terms, this maximum distance corresponded with the distance between the ends of the three stems (**Figure B.3.7**). Consistent with the SAXS data and our MD simulations, we predicted that $d=49.8 \pm 1.6 \text{ \AA}$ for the cocaine-free state, and $d=54.5 \pm 2.2 \text{ \AA}$ for the cocaine-bound state. This confirmed that the 3D structure of the MN4 aptamer became more oblate upon binding to cocaine.

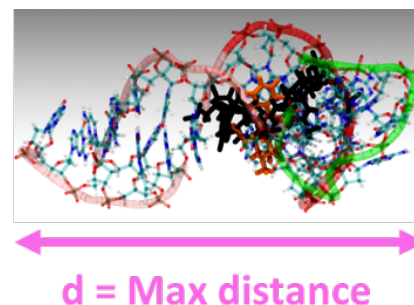


Figure B.3.7. Side view of the MN4 aptamer in the cocaine-bound state, defining the longest point-to-point distance, d . Stems 1-3 are shown in pink, green and red respectively. Cocaine and the junction bases are shown in orange and black respectively. Water and ions not shown for clarity.

We then sought to elucidate the molecular scale mechanism that may be driving this prolate-to-oblate conformational transition of the MN4 aptamer in the presence of cocaine. To do this, we predicted and

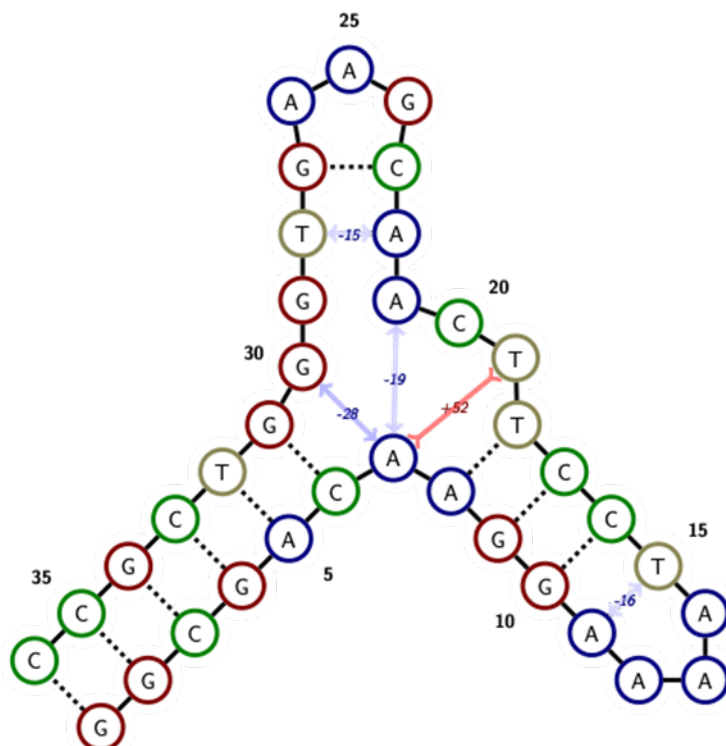


Figure B.3.8. Changes in our predicted hydrogen bonding in MN4 due to binding with cocaine in the central junction. Blue indicates a weakening of hydrogen bonds, orange indicates a strengthening of hydrogen bonds.

be explained below, this weakening can be explained by a diversion of these bases from base pair interactions into base-cocaine interactions. However, we also noted significant changes in a number of conventional base pair hydrogen bonds that were located some distance away from the central junction, namely A22-T28 (Stem 3) and remarkably, A11-T15 (Stem 2). In each case we show (herein) that these bases were not involved in any direct interactions with cocaine. This suggests that binding of a target analyte to a particular binding pocket may give rise to non-local conformational changes in the aptamer that are located far away from the binding site.

We next characterized the interactions between the aptamer and cocaine in the cocaine-bound state. To quantify this contact, we defined the centre of each base, and the centre of the cocaine phenyl ring, to

characterized the change in the hydrogen bonding distribution in MN4 before and after the binding of the cocaine molecule. These predicted changes in hydrogen bonding are illustrated in **Figure B.3.8**. The key message conveyed by these data is that the presence of cocaine leads to weakening of hydrogen bonds between some base pairs (particularly, but not exclusively, in the non-conventional base pairs) and strengthening of other base pairs. These weakening/strengthening effects effectively led to a concerted expansion/contraction of base-base distances, and thus can explain the spatial distortion of the aptamer when cocaine is bound to the central junction. Specifically, we noted weakening of the unconventional A7-G30 and A7-A21 base pairs in the junction region. As will

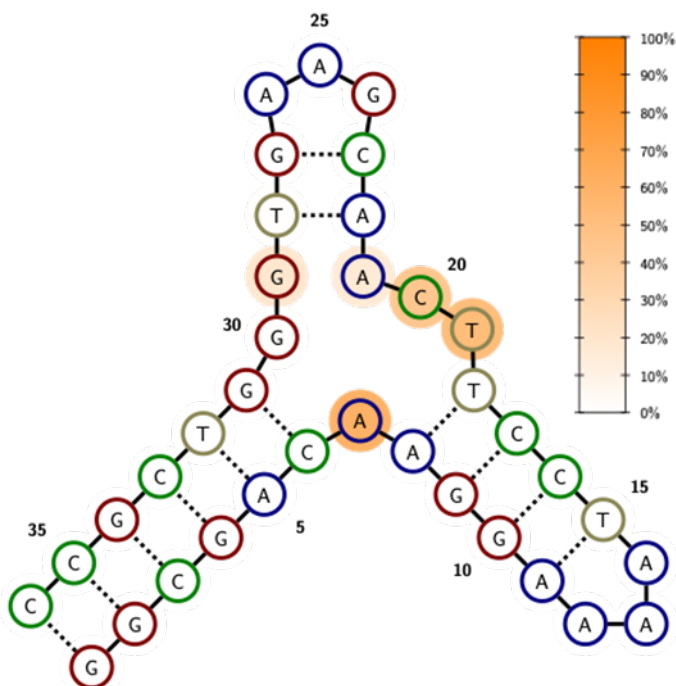


Figure B.3.9. Map of predicted aptamer-cocaine contact, averaged over all molecular dynamics simulations of the MN4-cocaine complex. Color-scheme indicates the average likelihood of contact to be present between a given cocaine-base pair, where 100% = always present, 0% = never present.

be reference sites, and we calculated the distances between all possible pairs of base-cocaine reference site in each frame of all of our MD simulation trajectories. We defined a given base-cocaine pair to be “in contact” when the distance between reference sites was 6 Å or less. Our findings, summarized in **Figure B.3.9**, indicate that the junction bases A7, T19, T20, and to a lesser extent, A21 and G29, were all involved in cocaine interactions, at least with the cocaine head group. Some of these bases were also found to be associated with the conformational distortion of MN4 in the cocaine-bound state, due to the concerted expansion and contraction of base-pair interactions in this region. We therefore propose that the participation of these bases in the binding of cocaine could credibly give rise to the observed expansion/contraction of base-pairings, and therefore drive the prolate-to-oblate conformational change of MN4. The participation of these bases in binding to cocaine is also consistent with the experimental findings of Neves *et al.*

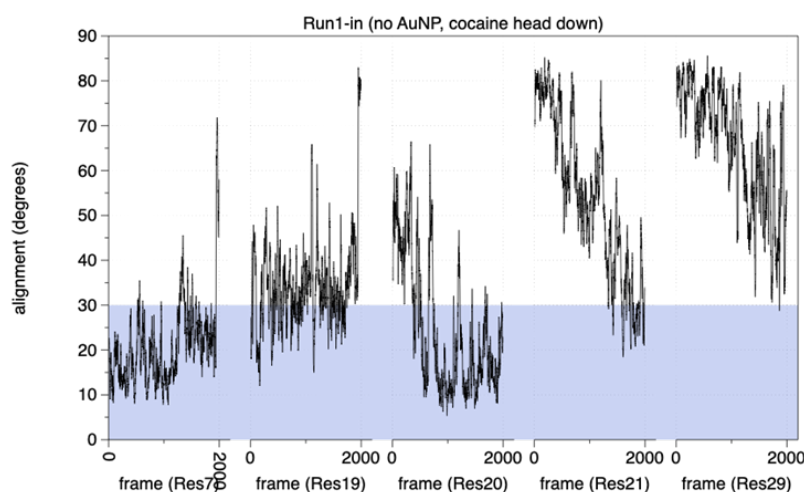


Figure B.3.10. Exemplar time-dependence of the orientational alignment of junction bases A7, T19, T20, A21 and G29 in MN4 with the cocaine aromatic ring. The grey shaded area indicates values of strong alignment (30 degrees or less), showing that A7, T19 and T20 are simultaneously aligned with cocaine in this case. Data taken from the last 2 ns of our production trajectories.

The nature of the interaction between the bases and the cocaine head was further probed by measuring the alignment of the orientation of the base when it was in contact with the cocaine head. We found that the presence of the aromatic cocaine head induced a concerted and simultaneous orientational alignment of several of the bases in the central junction region. As illustrated for an example case of one of the head-first simulations (**Figure B.3.10**), we found that in this particular case, bases A7, T19, and T20 were all substantially

aligned with the cocaine head group. In some extreme instances, all five bases were predicted to be simultaneously orientationally aligned with cocaine. We suggest that this concerted and simultaneous orientational alignment also contributes to the concerted expansion/contraction of the base pairings in the junction, and thus the conformational distortion of MN4 in the presence of cocaine.

In summary, we have successfully used molecular dynamics simulations to predict and elucidate the conformational response of the MN4 aptamer in response to binding of cocaine. Our predictions are consistent with the limited experimental data on these systems. Beyond the tentative hypotheses proposed by previous NMR studies, **our findings comprise the first such molecular-level explanation of this cocaine-induced conformational response of MN4.** These outcomes will provide a rational platform for the future design and implementation of aptamers as biorecognition elements in biosensing platforms.

B.4. Conformational disruption of the MN4 aptamer adsorbed on Au nanoparticle in the presence and absence of cocaine.

Recent investigations of the performance of the cocaine-binding MN4 aptamer as a biorecognition element in colorimetric sensors has been reported by AFRL researchers (Mirau *et al.* Ref 3). The biotic/abiotic interface in this sensor system comprises the interface between the MN4 aptamer and the Au nanoparticle, in aqueous salt solution. These researchers used structural NMR studies and binding assays to probe this MN4/AuNP interface. Their findings suggest that the MN4-cocaine interaction is much stronger than the MN4/AuNP non-bonded interaction. These authors also reported their NMR spectra for the MN4/cocaine complex were extremely similar to (almost identical with) the corresponding spectra for the MN4/AuNP/cocaine complex. This might suggest that the adsorption of the MN4/cocaine complex onto the Au surface gives rise to negligible further perturbations of the MN4 structure. Furthermore, on the basis of their NMR data, these authors proposed that bases in Stem 2 were principally involved in the MN4/AuNP interaction in the cocaine absent state, and that the binding of cocaine to MN4 may lead to weakening and ultimately desorption of the MN4/cocaine complex from the AuNP surface.

Based on our fundamental work presented in **Section B3**, herein we summarize the outcomes and analysis of molecular dynamics (MD) simulations to investigate these proposed mechanisms at the molecular level.

Methodology

Generation of the initial aptamer-nanoparticle

structures: We used our structure of the MN4 aptamer derived from our in-solution MD simulations (**Section B3**).

We used an approximately spherical Au NP with a diameter of ~ 5nm. Due to computing resource realities, this size represents the maximum size we could practicably consider. We constructed several different input structures where the MN4 aptamer was placed close to the surface of the Au NP. The “Junction Up”

initial configurations positioned the central junction (*i.e.* the cocaine binding site) away from the NP surface, while “Junction Down” configurations placed the central junction adjacent to the NP surface, as illustrated in **Figure B.4.1**. “Loop 2 Down” initial configurations were also explored, where Stem 2 (particularly dA12-dA14) was placed in contact with the Au surface. These simulations included negatively-charged citrate molecules adsorbed on the Au NP surface, in addition to Na⁺ counter-ions to counter-balance the total negative charge on the DNA. Further Na⁺ and Cl⁻ ions were added to ensure a 25 mM NaCl concentration. For each initial configuration, again we ran our simulations in triplicate (three independent simulations each), resulting in a total of six production simulations for the cocaine-free MN4/AuNP system. We also performed simulations of the MN4/cocaine/AuNP system, and herein we report the outcomes of four such independently generated simulations. We emphasize here that we set up these ternary system simulations by placing the MN4/cocaine complex (structures taken from our work summarized in **Section B3**) close to the AuNP surface. We ran all of our simulations in the isothermal-isobaric ensemble at a temperature of 300 K and a pressure of 1 atm.

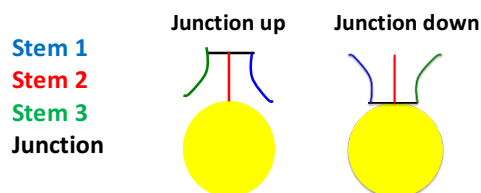


Figure B.4.1. Schematic of the initial configurations used in the cocaine-free MN4/Au nanoparticle simulations. The yellow circle represents the Au nanoparticle.

Results and Discussion

We start with our predicted structure of the cocaine-free MN4 aptamer adsorbed on the AuNP surface in salt solution, shown in **Figure B.4.2**. We found that both junction-down and junction-up configurations were stable, with the cocaine-free MN4 aptamer remaining in close contact with the AuNP surface for the majority of the simulations.

Following a similar set of analyses as reported for the cocaine-free MN4 aptamer in the absence of the AuNP (**Section B.3**), we first calculated the average radius of gyration of the cocaine-free aptamer in the surface-adsorbed state. For convenience of comparison, we re-state our R_g values for the unadsorbed (AuNP-free) MN4 in the absence and presence of cocaine as $15.6 \pm 0.3 \text{ \AA}$ and $17.2 \pm 0.3 \text{ \AA}$ respectively (in good agreement with experimental SAXS data). For the AuNP-adsorbed case, we found that adsorption of cocaine-free MN4 on the AuNP surface led to an overall average R_g of $16.9 \pm 0.3 \text{ \AA}$. There was very little difference in R_g when we examined the dependence of the adsorption geometry, given that the average Junction-up $R_g = 17.1 \pm 0.3 \text{ \AA}$ and the average Junction-down $R_g = 16.7 \pm 0.3 \text{ \AA}$. These data indicate that, compared with the R_g of the AuNP-free cocaine-free MN4 aptamer, adsorption on the AuNP surface leads to an increase in the spatial extent of the MN4 molecule. This suggests that adsorption on the AuNP surface in the absence of cocaine gives rise to a

conformational change that confers a similar effect to that of the effect of adding cocaine alone. In other words, whether MN4 binds cocaine, or adsorbs onto the AuNP surface, it appears to lead to a similar conformational outcome. We probed this further by analyzing R_g for our MN4/AuNP/cocaine simulations. In this instance, the average R_g was also found to be $16.9 \pm 0.3 \text{ \AA}$. This suggests that the two effects do not combine in an additive fashion to give rise to any further conformational distortion of the MN4 aptamer. As described in **Section B3**, to check if this change in R_g value was a consequence of the prolate-to-oblate conformational transition reported for MN4-cocaine binding, we also calculated the average "longest point-to-point" distance in the AuNP-adsorbed cocaine-free MN4 aptamer (denoted as d), which was found to be $54.2 \pm 1.3 \text{ \AA}$. For reference, the baseline AuNP-free cocaine-free MN4 d value was predicted to be $49.8 \pm 1.6 \text{ \AA}$, while the AuNP-free cocaine-bound MN4 d value was predicted to be $54.5 \pm 2.2 \text{ \AA}$. This confirms that the prolate-to-oblate rearrangement is also a feature of the cocaine-free MN4 upon adsorption onto the AuNP surface. In other words, the 3D umbrella-like structure of cocaine-free MN4 flattens somewhat upon AuNP adsorption. This is almost identical to the conformational outcome of AuNP-free MN4 binding cocaine alone. We also checked the conformational change for AuNP-adsorbed cocaine-bound MN4, and found an average d value of $53.8 \pm 1.4 \text{ \AA}$. Again, these data suggest that both AuNP adsorption and cocaine binding together do not lead to any additive enhancements in the conformational change.

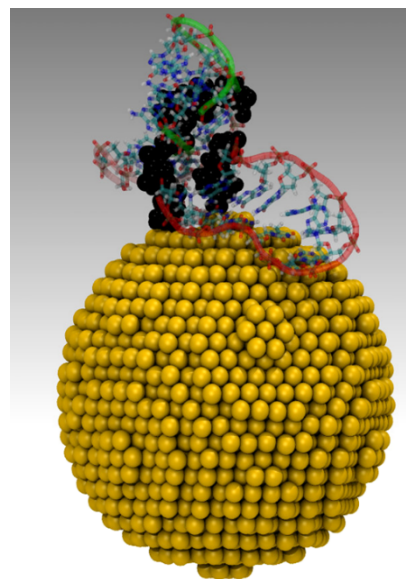


Figure B.4.2. Exemplar predicted structure of the cocaine-free MN4 aptamer adsorbed on the Au nanoparticle in salt solution. Water and ions not shown for clarity. Stems 1, 2, and 3 are shown in pink, red and green respectively. Junction bases are shown in black.

We next predicted the changes in the cocaine-free MN4 base pair hydrogen-bonding pattern upon adsorption onto the AuNP surface (**Figure B.4.3**). These changes in the hydrogen-bonding pattern are more complex than those predicted for the difference between AuNP-free MN4 in the cocaine-free and cocaine-bound states (shown in **Figure B.3.8**). One chief difference between **Figures B.3.8 and B.4.3** appear to be in the **Stem 2** region, where both expansion and contraction of hydrogen-bonded base pair contacts is evident upon adsorption to the AuNP. This was a key finding regardless of the adsorption orientation of MN4. In other words, this outcome held for both Junction-up and Junction-down simulations. One key similarity between **Figures B.3.8 and B.4.3** appears in the central junction region. However, the range of bases affected by AuNP adsorption is indicated to be wider than the range bases affected by cocaine binding alone. Specifically, the junction-relevant bases C6, A7, A8, T18,

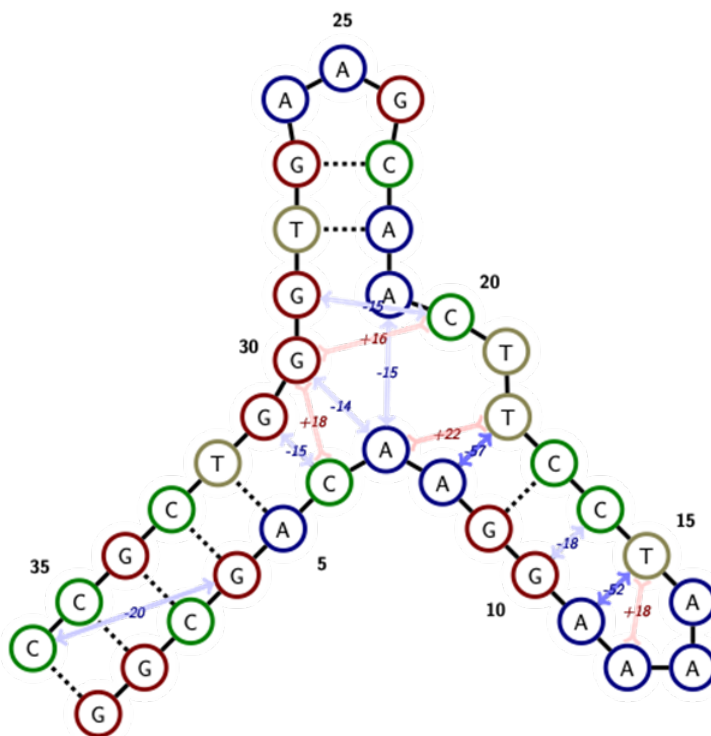


Figure B.4.3. Changes in the predicted average hydrogen bonding pattern in cocaine-free MN4 due to adsorption on the AuNP surface, relative to the AuNP-free state. Blue indicates a weakening of hydrogen bonds, orange indicates a strengthening of hydrogen bonds.

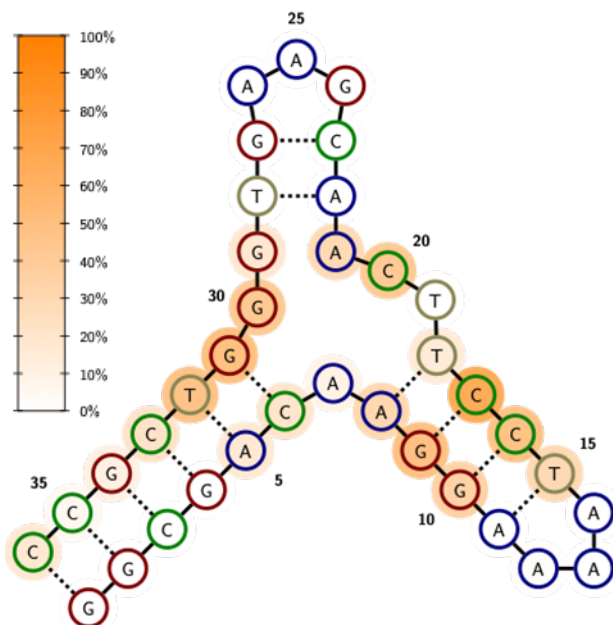


Figure B.4.4. Map of the average predicted contact between the cocaine-free aptamer and the Au nanoparticle. Color-scheme indicates the average likelihood of contact to be present between a given the nanoparticle surface and each base, where 100% = always present, 0% = never present.

C20, A21 G29, G30 and G31 were all affected by AuNP adsorption. In summary, despite the fact that AuNP adsorption gives rise to a similar flattening conformational effect in MN4 compared with cocaine binding alone, the impact on the hydrogen-bonding pattern appears to be more widespread, particularly with reference to **Stem 2**. However, this relatively more complex pattern of concerted expansion and contraction of hydrogen-bonded inter-base contacts led to an outcome similar with the cocaine-bound MN4 (in the absence of the AuNP); namely a flattening of the 3D umbrella structure.

Following this, we characterized the average degree of contact between cocaine-free MN4 in the AuNP-adsorbed state. To do this, we calculated the distance between the centre of every base and the nearest Au atom, for every frame in all of our production trajectories. We counted a base to be “in contact” with the AuNP surface if this distance was 5 Å. These data, summarized in **Figure B.4.4**,

indicate that **Stem 2** of MN4 was the main contact point with the AuNP surface, notably via bases A8, G9, G10, T15, C16, C17 and T18. The junction bases C20, A21, G29, G30, G31 also featured contact with the AuNP, in addition to the conventional **Stem 1** base pair A5-T32. The participation of bases in the central junction in adsorption to the AuNP suggests that addition of the cocaine molecule will lead to a competition between surface adsorption and binding to cocaine.

To investigate the competition between these two binding events, we calculated the average contact between the cocaine-bound MN4 aptamer and the AuNP surface. These data, shown in **Figure B.4.5**, indicate a general weakening in the overall contact with the AuNP surface, compared with the cocaine-free MN4 contact map in **Figure B.4.4**. This overall weakening takes into account a slight increase in the contact between **Stem 3** and the AuNP surface. The reduction in the surface contact with the junction bases can be explained by the dominance of the cocaine interaction in diverting these bases into cocaine-binding as opposed to surface binding. This suggests that the MN4-cocaine contact is stronger than the MN4-AuNP contact. This prediction from our simulations is consistent with the experimental findings reported by Mirau *et al.* We take this as evidence of incipient weakening of the MN4-

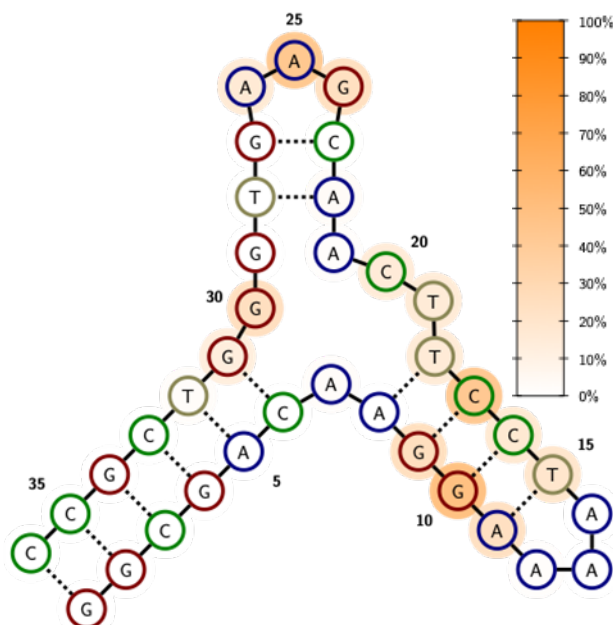


Figure B.4.5. Map of the average predicted contact between the cocaine-bound aptamer and the Au nanoparticle. Color-scheme indicates the average likelihood of contact to be present between a given the nanoparticle surface and each base, where 100% = always present, 0% = never present.

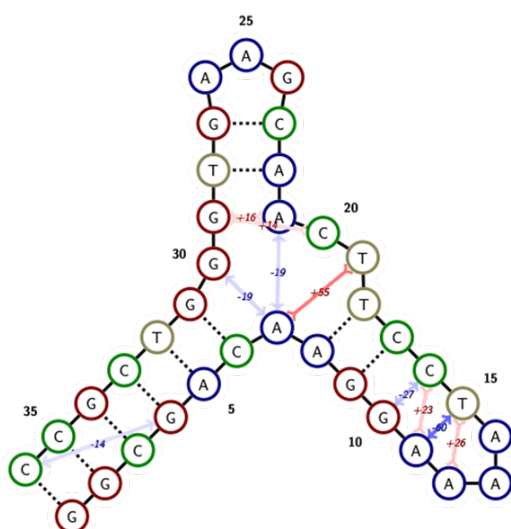


Figure B.4.6. Changes in the predicted average hydrogen bonding pattern in cocaine-bound MN4 due to adsorption on the AuNP surface, relative to the AuNP-free state. Blue indicates a weakening of hydrogen bonds, orange indicates a strengthening of hydrogen bonds.

AuNP interaction, and suggest that the degree of weakening exhibited in our simulations would have increased in severity if we had the capacity to undertake longer simulations. Ultimately, the ability to predict the free energy of interaction between MN4 and the nanoparticle, in the cocaine-free and cocaine-bound states, would be the ideal approach to test this. However, this strategy is currently not viable using current supercomputing capabilities.

In a similar vein, as described earlier in terms of predicted *R_g* values, we found that the 3D umbrella structure of the aptamer was flattened in the case of the cocaine-bound MN4 adsorbed on the AuNP surface. We found a similar molecular-scale cause for this flattening as we found for both the AuNP-free cocaine-bound MN4, and the cocaine-free AuNP-bound MN4.

To elaborate, we again found a concerted pattern of contraction and expansion of inter-base hydrogen bonds in cocaine-bound AuNP-bound MN4. These data are shown in **Figure B.4.6**. This pattern is very similar to what we reported in **Figure B.3.8** for AuNP-free cocaine-bound MN4, with the difference of some additional expansion/contraction in **Stem 2**. Again, this underscores that the structural perturbation of MN4 caused by the presence of the AuNP is negligible compared with the perturbation caused by the binding of the cocaine.

Finally, the dominance of the cocaine-MN4 interaction, relative to the AuNP-MN4 interaction, was also underscored by our prediction of the cocaine-MN4 contact map in the AuNP-adsorbed state. This map was found to be almost indistinguishable with the cocaine-MN4 contact map in the absence of the AuNP (data not shown). This suggests that the presence of the AuNP exerts a negligible influence on the ability of the MN4 aptamer to bind the cocaine analyte.

In summary, we have successfully used molecular dynamics simulations to predict the structure and binding properties of the MN4 aptamer in response to adsorption on an Au nanoparticle. We found that the cocaine-free MN4 aptamer formed strong contacts with the Au nanoparticle surface, with the bulk of the contacts formed between the nanoparticle and Stem 2. Our analysis supports the hypothesis that the MN4-cocaine interaction is much stronger and more dominant than the MN4-nanoparticle interaction, which can be used to explain the experimentally-observed cocaine-induced desorption of the MN4 from the nanoparticle surface. Our predictions are consistent with the experimental findings of AFRL researchers Mirau and co-workers and **provide the first such molecular-level explanation of the operation of MN4 in this colorimetric sensor**. These outcomes will provide a rational platform for the future design and implementation of aptamers as biorecognition elements in biosensing platforms.

C. Summary and Outlook.

In summary, we have made substantial progress in this project over the past two years. **First**, we confirmed that our all-atom force-fields are able to appropriately capture the interactions between DNA and relevant substrates, notably graphene and Au (both flat and NP surfaces). **Second**, we have completed simulations that can predict the in-solution and graphene adsorbed structures of an adenosine-binding aptamer that has been extensively characterized in terms of 3-D structure (in the un-adsorbed state). These two steps provided a solid foundation for investigating the structure of the MN4 DNA aptamer, which lacks a 3-D set of atomic coordinates, and for which limited information is publicly available regarding the structure of this aptamer when adsorbed at the aqueous Au NP surface.

Third, this project has provided the first 3D molecular coordinates of the MN4 aptamer in aqueous solution, in a bound complex with cocaine, when adsorbed onto a Au nanoparticle, and when complexed with cocaine in the nanoparticle-adsorbed state. Our molecular dynamics simulations have elucidated the molecular-scale mechanism of aptamer conformational change in response to binding cocaine and in response to adsorbing onto the nanoparticle surface. Our simulation data also explain why the cocaine-bound MN4 aptamer can desorb from the Au nanoparticle surface. Ultimately, these

simulations provide a credible foundation for future aptamer design, to ensure that aptamers can be adapted effectively to work in a range of challenging sensor environments.

While not summarized in **Section B4**, we did test loading effects – i.e. the influence of the presence of more than one MN4 aptamer adsorbed on the Au NP surface at the same time. These loading tests suggested that our predicted structures in the adsorbed state did not substantially differ with those predicted for the singly-adsorbed MN4/AuNP system. Also, in light of the surface curvature effects revealed by our previous simulations, we are also in the process of realizing a strategy to model a Au NP with a diameter of 10 nm, as a way to provide a structural model that is closer to that examined experimentally. The problem with modeling a solid 10 nm Au NP is that results in an extremely large number of atoms, so large that the simulations become impracticable. Therefore, we are testing the use of a partially hollowed-out 10 nm Au NP, such that the interior surface of the hollow NP is held fixed in space (the first atomic layer only). By removing most of the interior NP atoms, we can keep the number of atoms in our system down to a pragmatic level, to enable our MD simulations.

Finally, we have applied our new expertise, generated during this AOARD-funded project, to initiate a new modelling study of a very challenging aptamer system, namely the IgE (antibody)-binding aptamer [Ref 13]. This aptamer is thought to work in a redox-based or fluorescence-based sensing system, where a variant of this aptamer [Ref 14] is covalently attached to a Au nanoparticle surface. This aptamer is much larger than MN4 (70 nucleotides), and is thought to function via a large-scale conformational “molecular switching” rearrangement. This scenario makes an interesting contrast with our MN4 aptamer, where the conformational change upon binding to the target analyte leads to a much more modest conformational change. Our experimental collaborators at UNSW have identified that this aptamer fails to work properly under a broad range of general conditions. To investigate this, we have used molecular dynamics simulations to explore the potential ability of this aptamer to undergo such a large-scale conformational change when grafted to a nanoparticle surface at a given surface grafting density. Specifically, we have embarked on some molecular simulations of the aptamer-Au nanoparticle system that comprise a realistic grafting density (10 aptamers per 5 nm diameter nanoparticle). Our preliminary findings have uncovered unprecedented new insights into why these aptamers may not always function when taken from an un-tethered state and applied under operational conditions of a sensor; *i.e.* in a surface-adsorbed or surface-tethered state. In particular, we have found that the spatial concentration of placing 10 aptamers (each with -69 e of charge) into such a small volume gives rise to exceptional modifications of the solvent electrical double layer and solvent structuring, which can result in screening interactions. These “interaction screening” effects are their strongest at a distance from the nanoparticle surface that facilitates structural disruption of the key “switching” region of the aptamer. Our approach and insights are highly promising for helping to guide the design of similar systems such as the nanoflare project currently underway at AFRL.

References

1. Martin, J. A.; Chavez, J. L.; Chushak, Y.; Chapleau, R. R.; Hagen, J.; Kelley-Loughnane, N., Tunable stringency aptamer selection and gold nanoparticle assay for detection of cortisol. *Anal Bioanal Chem* **2014**, 406 (19), 4637-4647.
2. Wei, G.; Steckbeck, S.; Koppen, S.; Colombi Ciacchi, L. Label-free biosensing with single-molecule force spectroscopy. *Chem. Commun.* **2013**, 49, 3239–3241.
3. Barducci, A.; Bussi, G.; Parrinello, M. Well-tempered metadynamics: a smoothly converging and tunable free-energy method. *Phys. Rev. Lett.* **2008**, 100, 020603.
4. Wright, L. B.; Rodger, P. M.; Corni, S.; Walsh, T. R. GoIP-CHARMM: First-Principles Based Force-fields for the Interaction of Proteins with Au(111) and Au(100). *J. Chem. Theory Comput.* **2013**, 9, 1616-1630.
5. Hughes, Z. E.; Tomásio, S. M.; Walsh, T. R. Efficient simulations of the aqueous biointerface of graphitic nanostructures with a polarisable model. *Nanoscale* **2014**, 6, 5438–5448.
6. Hughes, Z. E.; Kochandra, R.; Walsh, T. R. Facet-Specific Adsorption of Tripeptides at Aqueous Au Interfaces: Open Questions in Reconciling Experiment and Simulation. *Langmuir* **2017**, 33, 3742-3754.
7. Lin, C. H.; Patel, D. J. Structural basis of DNA folding and recognition in an AMP-DNA aptamer complex: distinct architectures but common recognition motifs for DNA and RNA aptamers complexed to AMP. *Chem. Biol.* **1997**, 4, 817–832.
8. Z. J. Zhang, Oni, O.; Liu, J. W. New insights into a classic aptamer: binding sites, cooperativity and more sensitive adenosine detection. *Nucleic Acids Res.* **2017**, in press, DOI:10.1093/nar/gkx517.
9. Datta, D.; Meshik, X.; Mukherjee, S.; Sarkar, K.; Choi, M. S.; Mazouchi, M.; Farid, S.; Wang, Y. Y.; Burke, P. J.; Dutta, M.; Strosio, M. A. Submillimolar Detection of Adenosine Monophosphate Using Graphene-Based Electrochemical Aptasensor. *IEEE Trans. Nanotechnol.* **2017**, 16, 196–202.
10. Li, J.; Li, Q.; Colombi Ciacchi, L.; Wei, G. Label-Free Sensing of Adenosine Based on Force Variations Induced by Molecular Recognition. *Biosensors* **2015**, 5, 85–97.
11. Neves, M. A. D.; Reinstein, O.; Johnson, P. E., Defining a Stem Length-Dependent Binding Mechanism for the Cocaine-Binding Aptamer. A Combined NMR and Calorimetry Study. *Biochemistry*, **2010**, 49, 8478-8487.
12. P. A. Mirau, J. E. Smith, J. L. Chavez, J. A. Hagen, N. Kelley-Loughnane and R. Naik, *Langmuir*, **2018**, 34, 2139-2146.
13. T. W. Wigand, P. B. Williams, S. C. Dreskin, M. H. Jouvin, J. P. Kinet and D. Tasset, *J. Immunol.*, **1996**, 157, 221-230.
14. B. Y. Jiang, F. Z. Li, C. Y. Yang, J. Q. Xie, Y. Xiang and R. Yuan, *Anal. Chem.* **2015**, 87, 3094-30998.